Sources and variability of surface ozone over the Tibetan Plateau revealed by in situ observations and EMAC model simulations

Yihan Zou[1], Jianzhong Ma[1], Ningwei Liu[2], Weili Lin[3], Xiaobin Xu[1], Yunjia Li[1], Siyang Cheng[1], Xiangdong Zheng[1], Andrea Pozzer[4], and Jos Lelieveld[4]

[1]Chinese Academy of Meteorological Sciences, Beijing 100081, China
[2]Institute of Atmospheric Environment, China Meteorological Administration, Shenyang 110166, China
[3]Key Laboratory of Ecology and Environment in Minority Areas, Minzu University of China, National Ethnic Affairs Commission, Beijing 100081, China
[4]Atmospheric Chemistry Department, Max Planck Institute for Chemistry, Mainz, Germany

Correspondence to: Jianzhong Ma (majz@cma.gov.cn) and Xiangdong Zheng (xdzheng@cma.gov.cn)

Abstract. Ozone variability over the Tibetan Plateau (TP) is complex, and our understanding of the factors driving surface ozone variations on the plateau remains incomplete. We combine in-situ observations from the Nam Co (NMC) and Nepal Climate Observatory-Pyramid (PYR) stations with the global atmospheric chemistry-climate model EMAC to analyze the sources and spatiotemporal variations of surface ozone over TP. The three ozone source regions, i.e., the Northern Hemisphere and Tropical Stratospheric Source (NTST), Northern Hemisphere Mid-High Latitude Tropospheric Source (NHTS), and Tropical Tropospheric Source (TRTS), are considered. The results reveal strong seasonal and daily variability in the contributions of these sources to TP surface ozone. Regulated by the changes in the position and intensity of the subtropical westerly jet, surface NTST-O_3 is highest in spring, reaching a daily maximum contribution of 30% at both stations. The efficient transport of NHTS-O_3 by zonal circulation from source areas, including Central Asia, West Asia, and Europe, results in a summertime maximum of surface ozone in the northern TP, and even influences surface ozone on the central and southern TP, with a daily maximum contribution of 62% at NMC and 58% at PYR in summer. During the pre-monsoon period, enhanced TRTS-O_3 in South and Southeast Asia leads to annual surface ozone peaks in the southern and central TP, with a daily maximum contribution of 93% at NMC and 98% at PYR. With ongoing changes in the emissions of ozone precursors from the aforementioned areas, impacts on surface ozone over TP require continued investigation.

1 Introduction

Tropospheric ozone (O_3) is an important greenhouse gas, with a radiative forcing second only to carbon dioxide and methane (Myhre et al., 2013; Ramanathan et al., 1987). It is also a major source of hydroxyl radicals (OH), which controls the oxidizing capacity of the atmosphere (Lelieveld et al., 2016; Levy, 1971; Weinstock and Niki, 1972). As an oxidant and pollutant, elevated surface O_3 poses serious risks to human health and terrestrial vegetation (Desqueyroux et al., 2002; Lefohn et al., 2018; Shindell et al., 2012). Since the Industrial Revolution, increased global pollutant emissions driven by anthropogenic activities have resulted in a marked rise in tropospheric O_3 concentrations across many regions (Hough and Derwent, 1990; Monks et al., 2015; Vingarzan, 2004).

Stratospheric intrusion constitutes a significant source of tropospheric O_3 (Cristofanelli et al., 2003; Holton et al., 1995; Stohl et al., 2003; Tang et al., 2011). Typically, stratospheric intrusions are characterized by elevated O_3 concentrations at the tropopause and in the mid-troposphere, accompanied by high potential vorticity (PV) and low relative humidity (RH) (James et al., 2003; Kim and Lee, 2010; Zhao et al., 2021b). Stratospheric intrusion events are associated with upper-level jet streams. Seasonal variations in the frequency and intensity of these intrusions have been observed between low-latitude and mid-latitude regions, where jet stream activity is more pronounced (Ding and Wang, 2006; Ni et al., 2019). Long-term climatological analyses have identified the Tibetan Plateau as a global hotspot for deep stratosphere-to-troposphere exchange events, particularly during the boreal winter and spring (Škerlak et al., 2014). Due to its high elevation and correspondingly elevated boundary layer height, the Tibetan Plateau is recognized as a region where stratospheric O_3 intrusions exert a substantial impact on surface O_3 concentrations (Ding and Wang, 2006; Ma et al., 2002a; Yin et al., 2023).

Near-surface O_3 pollution episodes frequently occur in regions with substantial anthropogenic emissions of ozone-precursors. However, O_3 and its precursors can be transported over thousands of kilometers via atmospheric circulation, reaching even remote regions and thereby significantly altering the distribution of surface O_3 (Jacob et al., 1999). When O_3 and its precursors are transported from the boundary layer into the free troposphere by atmospheric circulation, their lifetimes are extended, allowing pollutants to be conveyed from sources in Europe, Asia, and North America to hemispheric and even global scales (Lelieveld and Dentener, 2000). Studies have shown that pollutants from North America can affect the central Atlantic within just 6 to 15 days, especially in spring and summer, contributing 3 to 5 ppb and 10 to 13 ppb to O_3 concentrations in Europe, respectively (Guerova et al., 2006). Trans-Eurasian pollutant transport also exerts a significant impact on O_3 concentrations in China and East Asia (Yoshitomi et al., 2011); while pollutants from India and the Middle East significantly affect O_3 concentrations in western China during the summer (Li et al., 2014). Within the Chinese domain, the Asian Summer Monsoon circulation transports pollutants from the southern to northern regions in eastern China, resulting in elevated regional background O_3 concentrations (Liu et al., 2020). Model simulations indicate that the Tibetan Plateau acts as a net sink for tropospheric O_3 in summer, with its surface O_3 primarily transported from the regions outside China (Ma et al., 2002a; Ma et al., 2002c).

Due to its sparse population and low level of industrialization, the Tibetan Plateau ranks among the cleanest regions on

Earth, and the spatiotemporal distribution of tropospheric O_3 over the plateau is primarily governed by dynamical transport (Ma et al., 2022). Long-term in situ measurements of surface O_3 on the Tibetan Plateau began at the Waliguan baseline station in 1994 (Ma et al., 2002b; Tang et al., 1995). Subsequent observations have shown significant differences in the seasonal variation characteristics of surface O_3 across different latitudes on the Tibetan Plateau, which have been categorized into two types: the spring maximum type and the summer maximum type (Ma et al., 2022; Yin et al., 2017). The Waliguan station in the northeastern Tibetan Plateau is a typical summer maximum type location, where surface O_3 exhibits a seasonal variation pattern with the maximum mostly occurring in summer and the minimum in winter (Ma et al., 2002b; Xu et al., 2016; Xu et al., 2018a; Zhu et al., 2004). In contrast, surface O_3 at the Nam Co Comprehensive Observation Station, Dangxiong Station, and Lhasa Station in the central Tibetan Plateau shows a regular seasonal cycle, with a maximum in spring (Lin et al., 2015; Ran et al., 2014; Yin et al., 2017). At the southern edge of the plateau, surface O_3 concentrations at the Nepal Climate Observatory-Pyramid (a global atmospheric background station) and China's Xianggelila Regional Atmosphere Background Station have an annual maximum during the pre-monsoon period (March-May),and a minimum during the summer monsoon season. This pattern is closely linked to the strong moisture transport and enhanced precipitation brought by the Asian summer monsoon (Cristofanelli et al., 2010; Ma et al., 2014).

Numerous studies have been conducted, and various mechanisms have been proposed to explain the causes of surface O_3 seasonal peaks at various stations on the Tibetan Plateau. For example, the summer O_3 peak at Waliguan has been attributed by some studies to frequent stratospheric intrusion events (Ding and Wang, 2006; Liang et al., 2008), while other studies suggest that it is influenced by air mass transport from central-eastern China, South Asia, Central Asia, and even Europe (Li et al., 2009; Xue et al., 2011; Zhu et al., 2004). Still others argued that it results from the combined effect of stratospheric intrusion and long-range transport from outside the region (Lee et al., 2007; Ma et al., 2002c; Xu et al., 2018a). Additionally, some studies have shown that the increase in surface O_3 at Waliguan in late spring is due to enhanced tropospheric photochemistry (Zheng et al., 2011). Recent research indicates that the monthly variability of surface O_3 across the Tibetan Plateau is largely controlled by stratospheric intrusion (Yin et al., 2023). Observational studies at Xianggelila Station and Nepal Pyramid Station have shown that abundant water vapor from the South Asian Summer Monsoon increases cloud cover and precipitation, significantly reducing surface O_3 concentrations during the summer (Ma et al., 2014; Marinoni et al., 2013; Putero et al., 2014).

While observational and modeling studies have confirmed the importance of stratospheric intrusions and dynamic transport to surface O_3 over the plateau, debate persists over the relative contributions of stratospheric intrusions versus long-range tropospheric transport for different sites and seasons. Furthermore, quantitative analyses of the sources of surface O_3 at individual stations lack consistent conclusions. Therefore, research integrating both observational and modeling evidence is needed to reduce these attribution uncertainties. Given that the central and southern Tibetan Plateau lies adjacent to the heavily polluted South Asian region and is significantly influenced by the South Asian monsoon, the sources and variability of surface O_3 in this area warrant further investigation.

Extensive in situ and satellite observations may provide information on the distribution and trends of tropospheric O_3

(Archibald et al., 2020; Tarasick et al., 2019). However, constrained by incomplete observational station coverage and the limited ability of satellites to detect surface O_3 (Hayashida et al., 2018), the understanding of the spatiotemporal distribution and variation mechanisms of O_3 across the globe is still incomplete, in particular over the Tibetan Plateau (Ma et al., 2022; Oltmans et al., 1996). Global atmospheric chemistry-circulation models can not only fill these observational gaps, but also help interpret observational results, revealing key processes and factors influencing O_3 distribution, variability and trends (Young et al., 2018).

This study aims to investigate surface O_3 sources and their variation characteristics in the central and southern Tibetan Plateau using measurements from two stations and ECHAM/MESSy atmospheric chemistry-climate model (EMAC) simulations. Section 2 presents basic information on the two stations located in the central and southern Tibetan Plateau and the EMAC model used in this study. Section 3 evaluates the EMAC model's simulation performance in reproducing surface O_3 variability at the two stations. Sections 4 and 5 present the contributions of stratospheric O_3 and tropospheric O_3 generated in different latitude bands to surface O_3 at the two stations, and examine the impacts of stratospheric O_3 intrusion and tropospheric O_3 transport from different source regions on surface O_3 over the Tibetan Plateau. Section 6 summarizes the conclusions of this study.

2 Observational stations and model description

2.1 Observational stations

The Nam Co Comprehensive Observation Station (30.77°N, 90.98°E, 4730 m above sea level, and hereafter referred to as NMC) is located between the southeastern shore of Nam Co Lake and the northern hills of the Nyainqêntanglha Mountains in the central and southern Tibetan Plateau (Figure 1). NMC experiences a dry and cold climate and is representative of typical alpine regions. The station is primarily influenced by three major synoptic systems: the South Asian Anticyclone, the subtropical high-pressure system, and southeastern warm and humid air masses. There are no concentrated industrial areas within a 100-kilometer radius of NMC, and even during the tourist peak season, local traffic is limited to a few vehicles passing through the area. Thus, the station is not locally influenced by major anthropogenic pollution sources (Xu et al., 2018b; Yin et al., 2017). For this study, surface O_3 was observed at NMC from 24 April 2011 to 14 July 2012.

The Nepal Climate Observatory at Pyramid (27.57°N, 86.48°E, 5079 m above sea level, and hereafter referred to as PYR) is situated at the confluence of the Lobuche and Khumbu glacier valleys (Figure 1). PYR is located on the southern edge of the Tibetan Plateau, with tundra as its primary vegetation cover. The air masses at PYR are strongly influenced by synoptic-scale circulations and local mountain winds, and thus by the transition between the summer and winter monsoons. PYR is remote from major anthropogenic pollution sources, with only small villages along the valley; the nearest major urban area is Kathmandu, approximately 200 km to the southwest (Bonasoni et al., 2008; Bonasoni et al., 2010; Cristofanelli et al., 2010). PYR is one of the 32 baseline stations within the World Meteorological Organization (WMO) Global Atmosphere Watch (GAW) programme. The surface O_3 data for PYR used in this study were obtained from the World Data

Centre for Reactive Gases (WDCRG), which serves as the central repository and archive for reactive gas data under the WMO/GAW programme (https://ebas-data.nilu.no, last access: 12 November 2024). For this study, the surface O_3 data at PYR span from 1 January 2010 to 31 December 2012.

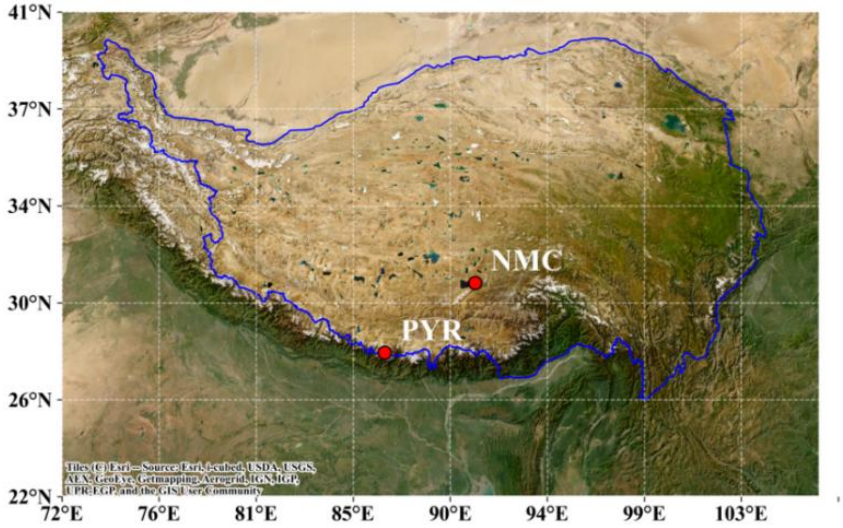

Figure 1. Location map of the NMC and PYR stations. The topographic background is provided by the ArcGIS World Imagery Map (https://doc.arcgis.com/en/data-appliance/6.4/maps/world-imagery.htm, last access: 23 May 2025). The blue lines refer to the 3000 m terrain height contour, highlighting the Tibetan Plateau. Sources: Esri, i-cubed, USDA, USGS, AEX, GeoEye, Getmapping, Aerogrid, IGN, IGP, UPR-EGP, and the GIS User Community | Powered by Esri.

2.2 Model description

The EMAC (ECHAM/MESSy Atmospheric Chemistry) model is an Earth system model that combines the fifth-generation general circulation model (ECHAM5), with the Modular Earth Submodel System (MESSy) (Jöckel et al., 2006; Jöckel et al., 2010). This model incorporates numerous submodels designed to simulate processes in the troposphere and middle atmosphere, as well as their interactions with the ocean, land, and human activities (Jöckel et al., 2005; Jöckel et al., 2010; Jöckel, 2016). EMAC has been widely applied in studies related to atmospheric chemical and climatic effects. Numerous studies have evaluated the EMAC model using observational data from surface stations, aircraft, and satellite measurements of trace gases and aerosols in both the troposphere and stratosphere (Eckstein et al., 2017; Jöckel et al., 2006; Kluge et al., 2023; Liu et al., 2020; Ma et al., 2019). By integrating processes such as chemical integral, physical processes, parameterization, and diagnostic calculations, the model system can effectively simulate complex dynamical, cloud, radiation, chemistry, emission, and deposition processes in the troposphere and stratosphere (Jöckel et al., 2005; Jöckel et al., 2010).

The EMAC model version used in this study is a combination of ECHAM5 version 5.3.02 and MESSy version 2.52. Detailed information on the modules and operational parameter settings used in the simulation can be found in Ma et al.

(2019); only a brief overview is provided here. The chemical kinetics module of EMAC employs the MECCA (Module Efficiently Calculating the Chemistry of the Atmosphere) gas-phase and heterogeneous chemical reaction module, which includes various chemical reactions that comprehensively describe the variations of O_3 and free radicals in the stratosphere and troposphere. Emission sources from fossil fuel combustion and biomass burning were simulated based on the Representative Concentration Pathways scenario 8.5 (RCP8.5) inventory (Jöckel et al., 2016). The RCP emission inventories have been used within the global atmospheric chemistry–climate model simulations in support of World Meteorological Organization (WMO)/United Nations Environment Programme (UNEP) ozone and International Global Atmospheric Chemistry (IGAC) climate assessments (Jöckel et al., 2016). The RCP8.5 global emission inventory has a horizontal grid resolution of 0.5° by 0.5° at monthly intervals and vertical distributions as described in Pozzer et al. (2009), and it is a reasonable choice for anthropogenic emissions over the period from 2000 to 2010 (Granier et al., 2011; Pozzer et al., 2015). The monthly RCP8.5 emissions in 2010 are used in this study.

The model spectral resolution used in this study was T106L90, which corresponds to a horizontal grid resolution of approximately 1.125° × 1.125° and 90 vertical layers extending from the surface to an altitude of 0.01 hPa. The model simulation period spans from 2010 to 2012, with an integration time step of 6 minutes. In the simulation, the meteorology was nudged by Newtonian relaxation towards the European Centre for Medium-Range Weather Forecasts (ECMWF) operational analysis data (including temperature, vorticity, divergence, and surface pressure). This approach makes the simulation results closely match the actual atmospheric state and facilitates comparison with observational data. The simulation results were output at one-hour intervals for analysis.

We use the model lowest layer, which is approximately at 60 m above the ground level, for surface ozone analyses. In the EMAC model, the nearest grid point to NMC is located at 30.84°N, 91.13°E, with a topographic height of 4644 m, which is 86 m lower than the observational site altitude. This grid point is suitable for capturing the topographic characteristics of NMC. PYR is located on the southern edge of the Tibetan Plateau, where the terrain is steep and highly heterogeneous. At a model resolution of 1.125° × 1.125°, subgrid-scale topographical features and local dynamics cannot be fully resolved. The model grid cell closest to PYR (27.48°N, 86.63°E) has a terrain elevation of only 2307 m, resulting in a discrepancy of 2772 m relative to PYR's actual elevation, and therefore cannot represent PYR. We instead selected the neighboring grid cell at 28.60°N, 86.63°E, whose elevation (4865 m) is much closer to the station altitude and better captures the surrounding topographic setting. A comparison among the nearby candidate grid cells shows that the lower-elevation cell would produce even higher surface O_3, which would further increase the positive bias at PYR. We therefore regard the remaining PYR bias as a consequence of the model's limited ability to represent complex topography and local meteorology, rather than as a problem that can be removed by choosing a different nearby grid cell.

The EMAC model employs the O_3 source-tagging technique (O3_ORIG) to conduct tagging simulations of O_3 produced at 14 different latitude and altitude bands worldwide (Grewe, 2006; Jöckel, 2016; Roelofs and Lelieveld, 1997). The 14 O_3 tracer source regions defined in the model are illustrated in Figure S2. Each O_3 tracer is generated exclusively within its corresponding source region but is subject to chemical loss and transport throughout the entire simulation domain. Based on

a quantitative analysis of the relative percentage contributions of each source region to surface O_3 at NMC and PYR (Table S2), the 14 original source regions were consolidated into three broader categories, i.e., the Northern Hemisphere and Tropical Stratospheric Source (NTST), the northern mid-high latitude troposphere (NHTS), and the tropical troposphere (TRTS) (Figure S3).

3 Comparison between the model simulations and site observations

Figure 2 presents the variations in the observed and simulated surface O_3 mixing ratios as a function of time at NMC (April 2011-July 2012) and PYR (January 2010-December 2012). The observed surface O_3 mixing ratio at NMC exhibits significant interdaily variability, with a maximum of 24.7 ppbv and an average of 4.7 ppbv; this variability is most pronounced in summer (Figure 2a). The observed interdaily variation in surface O_3 at PYR is relatively smaller than at NMC, with a maximum interdaily difference of 17.9 ppbv and an average of 3.4 ppbv; the interdaily variability is also most pronounced in summer. One can see from Figure 2a that surface O_3 simulated by EMAC shows interdaily variation trends similar to the observations for both NMC and PYR. As shown in Figure S1, the EMAC simulated O_3 mixing ratios exhibit strong daily correlations with the observations at both NMC and PYR. The correlation coefficients (R) between the simulated and observed daily surface O_3 mixing ratios are 0.72 for NMC and 0.78 for PYR. It can be concluded that the model performs well in capturing the daily variability of surface O_3 at the two sites, with a tendency towards higher O_3 levels in late spring/early summer.

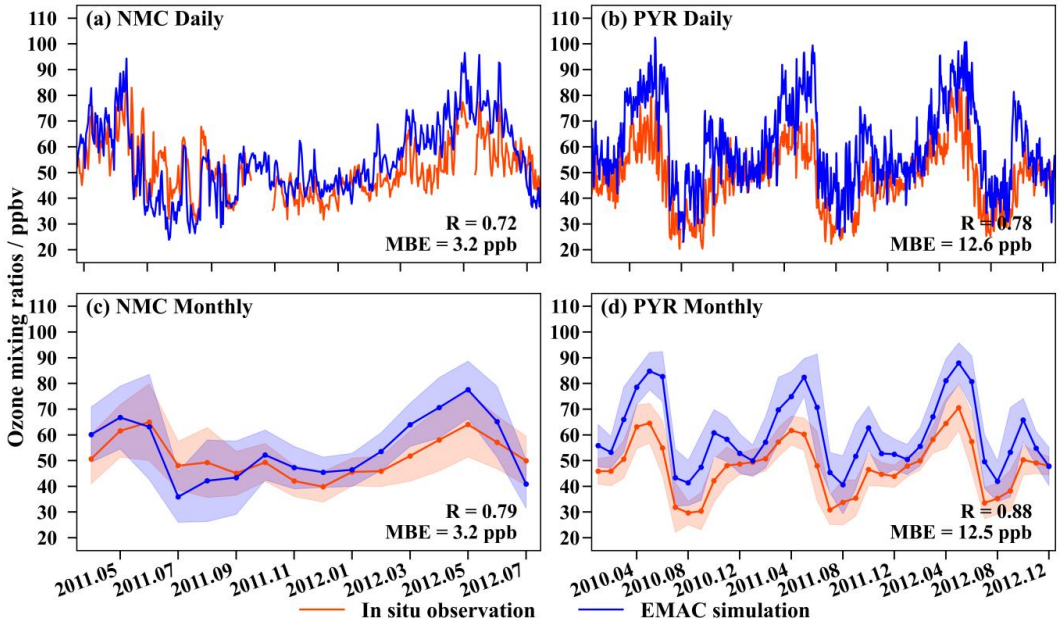

Figure 2. Comparisons between EMAC-simulated (blue) and observed (red) surface O_3 mixing ratios (ppbv) at NMC (April 2011 to July 2012; panels a, c) and PYR (January 2010 to December 2012; panels b, d), where panels (a, b) show daily time series and panels (c, d) show monthly time series.

Table 1 presents differences in the quantitative simulation accuracy of the EMAC model for surface O_3 mixing ratios at the two stations. A statistical analysis of observational data shows that during the observation period, the surface O_3 mixing ratio at NMC has a mean and standard deviation of 51.4 ± 10.8 ppbv, which is consistent with the range of 47.6 ± 11.6 ppb reported for the region by Yin et al. (2017). At PYR, the observed mean surface O_3 mixing ratio was 47.8 ± 12.4 ppbv (Figure 2b), which falls within the range of historical observations (49 ± 12 ppbv) reported by Cristofanelli et al. (2010). For the investigated period, the model-simulated daily surface O_3 mixing ratios at NMC have a mean bias (MB) of 3.2 ppbv, a normalized mean bias (NMB) of 6.1%, and a relatively small simulation error (root-mean-square error, RMSE = 10.9 ppbv). The simulated daily surface O_3 mixing ratios at PYR show an MB of 12.6 ppbv, an NMB of 26.3%, and an RMSE of 16.1 ppbv. This indicates a significant overestimation of surface O_3 at PYR by the model.

Table 1. Statistical comparison of observed and EMAC-simulated surface O_3 at NMC and PYR (daily and monthly scales)

Station name	Observed Mean ± Standard Deviation	Simulated Mean ± Standard Deviation	Time Scale	r	MB(ppbv)	RMSE(ppbv)	NMB(%)
NMC	51.4±10.8	54.8±14.7	daily	0.72	3.2	10.9	6.1
			monthly	0.79	3.2	7.7	6.6
PYR	47.8±12.4	60.3±16.1	daily	0.78	12.6	16.1	26.3
			monthly	0.88	12.5	14.1	26.2

Figure 2c and Figure 2d display the monthly variations in the surface O_3 mixing ratios at NMC and PYR, respectively. The surface O_3 mixing ratios at NMC exhibit a seasonal variation pattern characterized by the highest values in spring and the lowest in winter, while those at PYR show a yearly cycle with a maximum in spring and a minimum in summer. The correlation coefficients between the simulated and observed monthly surface O_3 mixing ratios are 0.79 for NMC and 0.88 for PYR (Table 1), indicating that the model has a strong capability to reproduce monthly-scale trends at the two sites. For the monthly surface O_3 mixing ratios, the EMAC model exhibits an MB of 3.2 ppbv and an NMB of 6.6% at NMC, and an MB of 12.5 ppbv and an NMB of 26.2% at PYR. The RMSE at PYR (14.1 ppbv) is nearly twice as large as the RMSE at NMC (7.7 ppbv).

The persistent positive bias at PYR indicates that the model tends to overestimate surface O_3 over the southern Tibetan Plateau, particularly during late spring and early summer when stratospheric influence and photochemical O_3 formation are strongest. Because the model performance at NMC is much better, the PYR bias is unlikely to arise from a uniform overestimation across the entire Tibetan Plateau. Instead, it likely reflects the difficulty of representing the complex topography, local wind systems, precipitation, and boundary-layer exchange at PYR, as well as potentially underestimated dry deposition (e.g., due to underestimated vegetated surfaces, also because the bias is largest in the growing season). While the bias affects the absolute magnitudes, the simulated seasonal cycles and relative source contributions remain robust.

Consequently, we interpret the PYR source contributions as physically meaningful within the current model configuration, while noting that their absolute magnitudes are subject to local terrain uncertainty.

4 Source attribution of surface ozone at NMC and PYR

~~Based on a quantitative analysis of the relative percentage contributions of each source region to surface O_3 at NMC and PYR (Table S2), the 14 original source regions were consolidated into three broader categories, i.e., the Northern Hemisphere and Tropical Stratospheric Source (NTST), the northern mid-high latitude troposphere (NHTS), and the tropical troposphere (TRTS) (Figure S3).~~

~~The daily relative percentage contributions from the Southern Hemisphere sources (SHTS, SMLS, SMUS, SPLS, SPUS) to surface O_3 at both stations were all below 1%; consequently, these Southern Hemisphere sources were ignored in the subsequent analysis. Previous studies have demonstrated that the contribution of stratospheric sources to surface O_3 over the Tibetan Plateau is not negligible (Cristofanelli et al., 2010; Ding and Wang, 2006; Ma et al., 2014; Škerlak et al., 2019). Accordingly, we retained stratospheric sources for analysis. However, as our study focuses on the overall contribution of stratospheric sources rather than the differences among stratospheric sources at different latitudes, we merged the seven stratospheric source regions (NMLS, NMUS, NPLS, NPUS, TRLS, TRMS, TRUS), each of which contributed less than 10% to the 3-year average percentage contributions at both stations individually, into a single source category, namely the Northern Hemisphere and Tropical Stratosphere (NTST). Notably, even after merging these stratospheric sources, the contribution of the combined NTST remains smaller than that of the tropospheric sources. We retained the two tropospheric source regions, i.e., the northern mid-high latitude troposphere (NHTS) and the tropical troposphere (TRTS), which exhibited relatively large 3-year average percentage contributions, both exceeding 15%.~~

4.1 Contributions from ozone generated in the stratosphere

Figure 3 presents the daily absolute contributions and relative contributions of O_3 generated from the three source regions to surface O_3 at NMC (30.77°N, located in the mid-latitudes of the Northern Hemisphere and central Tibetan Plateau) and PYR (27.57°N, located in the low latitudes of the Northern Hemisphere and southern Tibetan Plateau). Table 2 summarizes the average contributions of the three major sources to surface O_3 at NMC and PYR in different meteorological seasons~~ and monsoon phases~~. The temporal variation characteristics of NTST-O_3 at NMC (Figure 3a) are highly consistent with the seasonal cycle of surface O_3 at this site (Figure 2a). Values of NTST-O_3 at NMC are most prominent in spring, with a typical range of 10-25 ppbv (a relative contribution range of 10%-20%) and a maximum of 28 ppbv (a maximum relative contribution of 30%). The interdaily variation amplitude of NTST-O_3 at NMC is large, with a maximum of 15 ppbv. NTST-O_3 at NMC is notably smaller in summer than in spring. NTST-O_3 at NMC is lowest in autumn, with a maximum (and relative contribution) of only 7 ppbv (and 9%). The interdaily variation amplitude is also small in this season, with a maximum of 5 ppbv. In winter, NTST-O_3 at NMC ranges from 1 to 18 ppbv, with a maximum relative contribution of 30%.

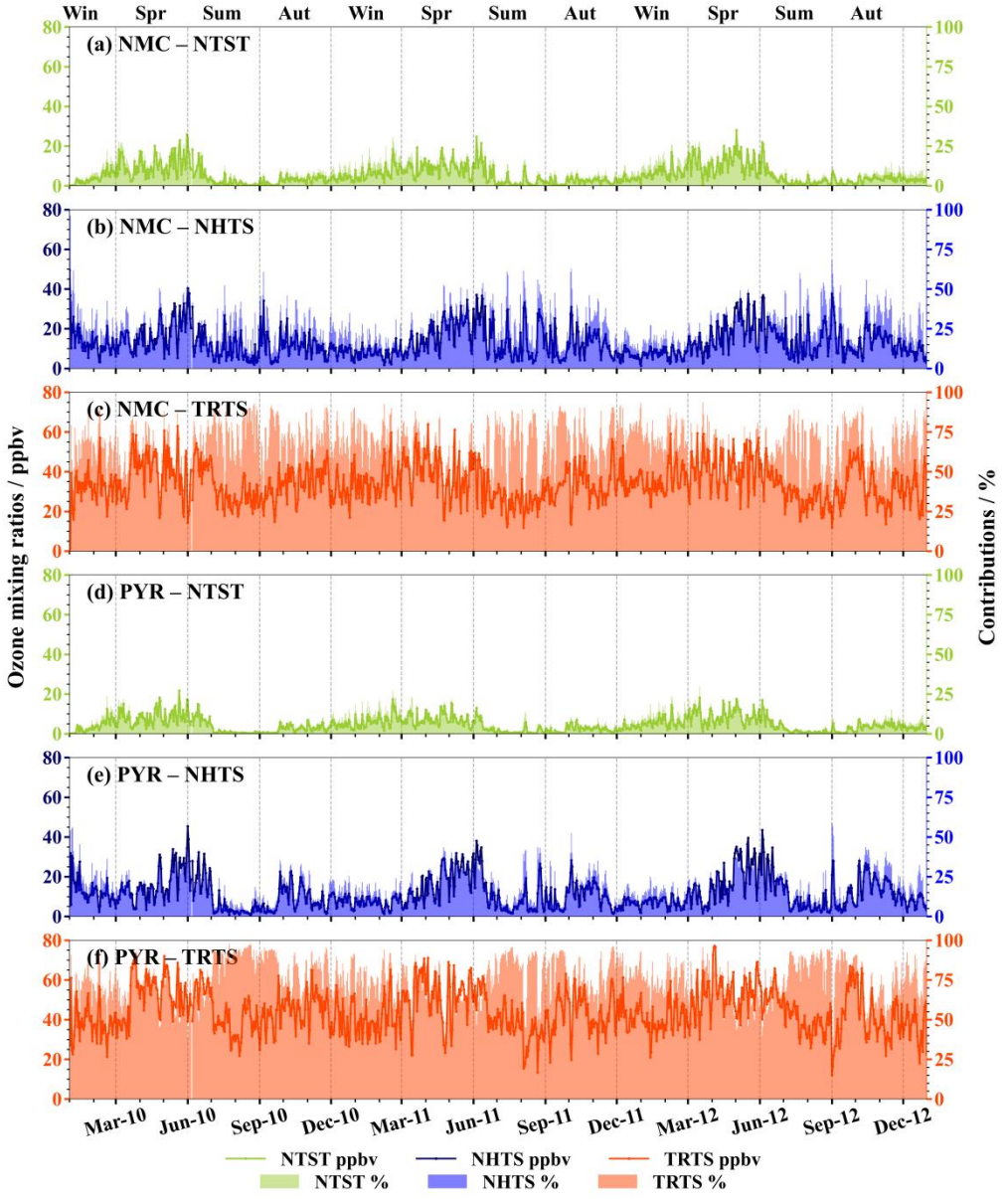

Figure 3. Daily absolute (solid lines) and relative (shaded bars) contributions of O_3 produced in the three source regions (TRTS: red, NHTS: blue, NTST: green) to surface O_3 at NMC (a, b, c) and PYR (d, e, f) during 2010–2012, simulated by the EMAC model.

Table 2. Average contributions of the three major sources to surface ozone at NMC and PYR stations in different seasons and monsoon phases.

Season	NMC			PYR		
	NTST-O_3 (ppbv)	NHTS-O_3 (ppbv)	TRTS-O_3 (ppbv)	NTST-O_3 (ppbv)	NHTS-O_3 (ppbv)	TRTS-O_3 (ppbv)
Spring	10.1	16.8	40.3	8.1	16.2	52.3
Summer	3.7	13.6	29.7	2.7	10.2	41.9
Autumn	2.7	12.4	33.2	2.6	10.6	43.2
Winter	4.9	9.6	33.4	4.7	8.8	39.7

As shown in Figure 3d, NTST-O_3 at PYR also exhibits a characteristic spring peak, with a maximum of 22 ppbv (corresponding to a relative contribution of 30%). The interdaily variation amplitude of NTST-O_3 at PYR is large, with a maximum interdaily difference of 11 ppbv. Under the influence of the monsoon circulation, NTST-O_3 at PYR drops to the lowest level in summer and autumn throughout the year. In winter, NTST-O_3 at PYR ranges from 1 to 17 ppbv, with a maximum relative contribution of 27%. Comparison between NMC and PYR reveals that the contribution of NTST-O_3 to surface O_3 features higher peaks and more pronounced fluctuations at NMC than at PYR, indicating that the mid-latitude location is more susceptible to stratospheric intrusion events.

4.2 Contributions from ozone generated in the troposphere

The NMC site is located in the Northern Hemisphere mid-latitudes ~~of the Northern Hemisphere~~, falling within the latitude range of the NHTS for O_3 sources in the model. The PYR site is situated in the low latitudes of the Northern Hemisphere, lying within the latitude range of the TRTS for O_3 sources in the model. Compared to the stratospheric source (NTST-O_3), the variations of O_3 from the two tropospheric sources (NHTS-O_3 and TRTS-O_3) are significantly influenced by the monsoon, showing distinct characteristics across different monsoon phases. Based on monsoon regularity, we divide the calendar year into four phases, the pre-monsoon period (March 1 to June 20~~March to mid-June~~), the monsoon period (June 21 to September 10~~late-June to early September~~), the post-monsoon period (September 11 to November 30~~mid-September to November~~), and the winter period (December to February of the following year).

Figure 3b shows that NHTS-O_3 at NMC ranges from 1 to 40 ppbv, with relative contributions ranging from 3% to 68%. During the pre-monsoon period, NHTS-O_3 at NMC is most prominent with a maximum of 40 ppbv, and the relative contribution ranges from 4% to 54%. In the monsoon period, NHTS-O_3 at NMC is slightly lower than that in the pre-monsoon period, but exhibits a large interdaily variation amplitude, with a maximum of 22 ppbv. Notably, although simulated O_3 level is at its minimum (Figures 2a and 2c), NHTS-O_3 at NMC has relatively high relative contributions (a peak

of 62%) in the monsoon period. During the post-monsoon period, the interdaily variation amplitude of the relative contributions of NHTS-O_3 at NMC is large, with a maximum of 40%. In winter, NHTS-O_3 at NMC ranges from 1 to 22 ppbv, with a relative contribution range of 3%-40%. The interdaily variation amplitude of NHTS-O_3 is much larger than that of NTST-O_3 at NMC, reflecting higher variability in transport of O_3 from the mid-to-high latitude tropospheric sources than from the stratospheric sources.

Figure 3e shows that NHTS-O_3 at PYR exhibits a large interdaily variation amplitude, with a maximum of 22 ppbv (and 38%) for the absolute (and relative) contributions. During the pre-monsoon period, NHTS-O_3 at PYR is most prominent, with a maximum absolute contribution of 45 ppbv and a relative contribution ranging from 2% to 45%. In the monsoon period, NHTS-O_3 at PYR decreases significantly to the lowest level of the year, with a maximum of 28 ppbv. However, despite its low absolute values, NHTS-O_3 at PYR still exhibits relatively high relative contributions (with a peak of 58%) during this period. During the post-monsoon period, NHTS-O_3 at PYR ranges from 1 to 28 ppbv (with a relative contribution range of 1%-52%). In winter, it ranges from 1 to 27 ppbv (with a relative contribution range of 2%-45%). Comparison between the two stations reveals that NHTS-O_3 at both sites exhibits large interdaily variation amplitudes, but the overall interdaily difference is larger at NMC than at PYR, indicating that transport of O_3 from the mid-high latitude tropospheric sources has a more prominent fluctuating impact on the interdaily variations of surface O_3 at NMC (mid-latitudes) than at PYR (low latitudes).

Figure 3c presents the variations in the contributions of TRTS-O_3 to surface O_3 at NMC. The interdaily variation amplitude of TRTS-O_3 at NMC is large, with a maximum of 22 ppbv (and 40%) for the absolute (and relative) contributions. During the pre-monsoon period, TRTS-O_3 at NMC is significantly higher than that in other periods, ranging from 15 to 64 ppbv. During the monsoon period, it decreases to 12-46 ppbv, which is significantly lower than in other periods. However, the relative contribution of TRTS-O_3 at NMC reaches the annual peaks during the monsoon period, with a maximum of 93%. TRTS-O_3 levels at NMC begin to recover in the post-monsoon period and during winter.

Figure 3f presents the variations in the contributions of TRTS-O_3 to surface O_3 at PYR. The interdaily variation amplitude of TRTS-O_3 at PYR is large, with a maximum of 30 ppbv (and 43%) for the absolute (and relative) contributions. During the pre-monsoon period, TRTS-O_3 at PYR is the highest, ranging from 22 to 77 ppbv. During the monsoon period, it decreases to 12-60 ppbv, which is significantly lower than in other periods. However, the relative contribution of TRTS-O_3 at PYR reaches the annual peaks during the monsoon period, with a maximum of 98%. Compared to NMC, TRTS-O_3 at PYR is generally higher and exhibits a greater peak contribution and a longer duration in the pre-monsoon period, indicating that TRTS-O_3 exerts a more direct and sustained impact on the low-latitude region of the Tibetan Plateau.

5 Surface ozone sources and variability at a larger spatial scale

In the above section, we have examined the contributions of O_3 from different source regions (NTST, NHTS, and TRTS) to the temporal variations of surface O_3 at the two stations (NMC and PYR). In this section, we conduct a detailed analysis of how O_3 from these three source regions influences surface O_3 variations at the two stations and across the Tibetan Plateau

through dynamics and transport.

5.1 Influences of ozone from the stratospheric sources

5.1.1 Seasonal patterns of surface ozone from the stratospheric sources

Figure 4 presents the regional distributions of surface NTST-O_3 and 200 hPa wind fields in different seasons averaged from 2010 to 2012. The corresponding distributions of the relative contribution of surface NTST-O_3 to total modelled O_3 are provided in Figure S4 in the Supplement. For the spring 200 hPa wind field (Figure 4a), the high wind speed center over the Tibetan Plateau is located within 29°N and 35°N, with the jet axis situated in the hinterland of the Tibetan Plateau. In spring, there are two high-value centers of NTST-O_3 with concentrations exceeding 10 ppbv over the central (82°E-93°E, 30°N-34°N) and northeastern (95°E-99°E, 36°N-40°N) Tibetan Plateau. This is consistent with the simulation results of Ye et al. (2024) using the GEOS-Chem High Performance global atmospheric chemistry model, which showed that the contribution of stratospheric O_3 to the background O_3 over the Tibetan Plateau exceeds 10 ppbv in spring (Ye et al., 2024). In spring, the NMC station is located within the high-value zone of surface NTST-O_3 mixing ratios, which is consistent with previous research findings (Lin et al., 2016; Yin et al., 2017). The subtropical westerly jet is often accompanied by the eastward propagation of Rossby waves. Due to the breaking of Rossby waves, large-scale downward motion occurs near the core of the subtropical westerly jet, generating strong vertical wind shear that is prone to inducing tropopause folding, thereby promoting the downward transport of stratospheric O_3 to the troposphere (Chen et al., 2011; Luo et al., 2019; Xu et al., 2018a; Xu et al., 2023; Yin et al., 2023; Zhao et al., 2021a; Zhao et al., 2021b). To quantify ~~the~~ dynamical transport processes related to~~from~~ the stratosphere, we calculated the tropopause fold frequency using~~based on~~ the 3D labeling algorithm refined by Škerlak et al. (2015). The air masses were classified by detecting multiple crossings of the dynamical tropopause interface, defined by the 2 PVU isosurface and specific humidity threshold (0.1 g/kg). Folds are characterized by their vertical extent (ΔP). In this study, instances with a pressure difference ΔP ≥50 hPa within the interconnected fold grids were cataloged as tropopause folding events to compute the seasonal occurrence frequencies~~.~~ (Figure S5). In spring, the region of maximum tropopause fold frequency is concentrated within the 28°N–34°N latitudinal band, where the occurrence frequency exceeds 35% and reaches a peak of 48% (Figure S5a). ~~As shown in Figures S6 and S7 in the Supplement, both the absolute concentrations and relative fractions of NTST-O_3 at the 200 hPa level (representing the lower stratosphere) reach their annual maximums in spring across the Northern Hemisphere Mid-High latitudes, providing an abundant source reservoir. The combination of the abundant lower stratospheric ozone reservoir and the high frequency of tropopause folding leads to the annual maximum of surface NTST-O_3 over the TP in spring.~~

In summer (Figure 4b), the subtropical westerly jet shifts northward (Schiemann et al., 2009), with the jet core located on the northern side of the Tibetan Plateau, and the frequent tropopause folding zone migrates to the northern edge of the plateau (Figure S5b). ~~Meanwhile, the 200 hPa NTST-O_3 background concentration drops to its annual minimum (Figure S6b).~~ Correspondingly, the high-value center of NTST-O_3 moves to the northwestern part of the plateau, and the overall

NTST-O_3 mixing ratio is lower than that in spring. Previous studies have indicated that the summer surface O_3 peak at Waliguan in the northeastern Tibetan Plateau is attributed to downward transport of O_3 from the upper troposphere and lower stratosphere (Ding and Wang, 2006; Ma et al., 2005). In autumn (Figure 4c), with the southward retreat of the jet stream and the significant decrease in tropopause fold frequency over the plateau (Figure S5c), ~~as well as a continuously low 200 hPa background concentration (Figure S6c)~~, the surface NTST-O_3 mixing ratio over the Tibetan Plateau drops sharply to the lowest value of the year, with surface NTST-O_3 across the entire plateau being lower than 5 ppbv. For the winter 200 hPa wind field (Figure 4d), the jet stream exhibits the strongest intensity during this season, and its center has retreated to the southern Tibetan Plateau, leading to a resurgence of tropopause folding events along the southern edge (Figure S5d). ~~Simultaneously, the 200 hPa NTST-O3 reservoir begins to accumulate significantly. The coupling of these factors leads to a slight increase in NTST-O_3 mixing ratio compared to that in autumn.~~, and the NTST-O_3 mixing ratio shows a slight increase compared to that in autumn.

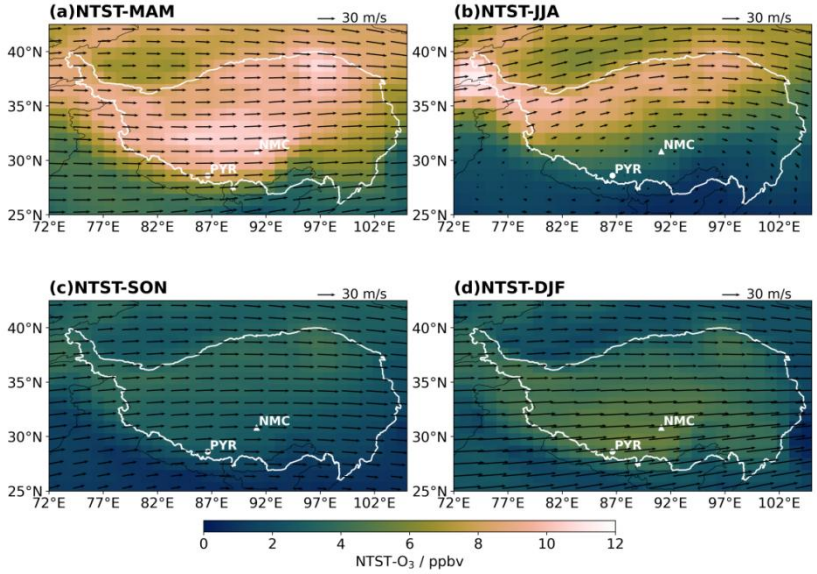

Figure 4. EMAC simulated regional distributions of surface NTST-O_3 and 200 hPa wind field over the Tibetan Plateau in different seasons during 2010–2012: (a) Spring, (b) Summer, (c) Autumn, (d) Winter. Color shading denotes NTST-O_3 volume mixing ratio (units: ppbv), and black arrows represent the wind field (units: m/s). White lines refer to the 3 km terrain height contour, highlighting the Tibetan Plateau area. White dots mark the locations of the PYR (circle) and NMC (triangle) stations.

In summary, changes in the position and intensity of the subtropical westerly jet constitute the key meteorological background regulating the seasonal differences in the influence of NTST-O_3 on the Tibetan Plateau. This background also helps explain the inter-station differences. NMC is located at the edge of the NTST-O_3 high-value center, indicating a higher contribution of stratospheric sources to surface ozone at NMC. In contrast, PYR is situated on the southern edge of the

plateau, affected by the topographic influence of the Himalayas on the one hand, and by the monsoon circulation in summer and autumn on the other. Thus, the overall influence of NTST-O_3 on PYR is smaller than that on NMC. Previous studies on the influence of stratospheric O_3 on the Tibetan Plateau often used screening methods designed based on in-situ observational data (such as O_3, RH, CO, total column ozone, PV, etc.) to identify stratospheric intrusion events (Chen et al., 2011; Cristofanelli et al., 2010; Ma et al., 2014), and these screening methods have certain limitations. Our tracer method clearly identifies the source regions of O_3 and can accurately reflect the impact of stratospheric source O_3 on the study area.

5.1.2 Analysis of stratospheric intrusion events

The aforementioned analysis demonstrates the seasonal variation and regional distribution characteristics of surface NTST-O_3 over the Tibetan Plateau. However, it cannot account for the frequently observed interdaily variability in surface NTST-O_3 at the stations during spring, which occurs on a shorter time scale, as presented in Section 4.1. To further reveal the physical mechanism underlying this rapid variation, we select an event in spring (4-5 March 2010), which shows a strong interdaily variability of NTST-O_3 at the stations, for case analysis (Figure 5). The temporal variations in the relative contribution of NTST-O_3 to total modelled O_3 during this event are illustrated in Figure S6 in the Supplement. This event was specifically chosen because both the absolute and relative contributions of NTST-O_3 at the sites exceeded the 95th percentile ~~of~~for the ~~entire~~ 2010 – 2012 period, representing a robust stratospheric intrusion.

On 4 March (Figure 5a), at the 200 hPa level, distinct high-NTST-O_3 zones appear in the mid-latitude belts over the northwestern (60°E-77°E, 33°N-39°N) and northeastern (89°E-115°E, 40°N-45°N) Tibetan Plateau, adjacent to the northern part of the westerly jet axis. The 200 hPa wind field shows that the high-wind speed center is located between 25°N and 33°N, and the wind direction shifts from southwest to northwest over the southeastern Tibetan Plateau. On 5 March (Figure 5b), the high-NTST-O_3 center over the northeastern region from the previous day is advected southeastward by the westerly jet stream, moving to the area above the northern Tibetan Plateau (71°E-98°E, 33°N-40°N), and the NTST-O_3 mixing ratio above the southern plateau also increases compared to the previous day. The 200 hPa wind field indicates that the span of the jet stream expands compared to the previous day, with the range of the jet axis extending to 23°N-35°N.

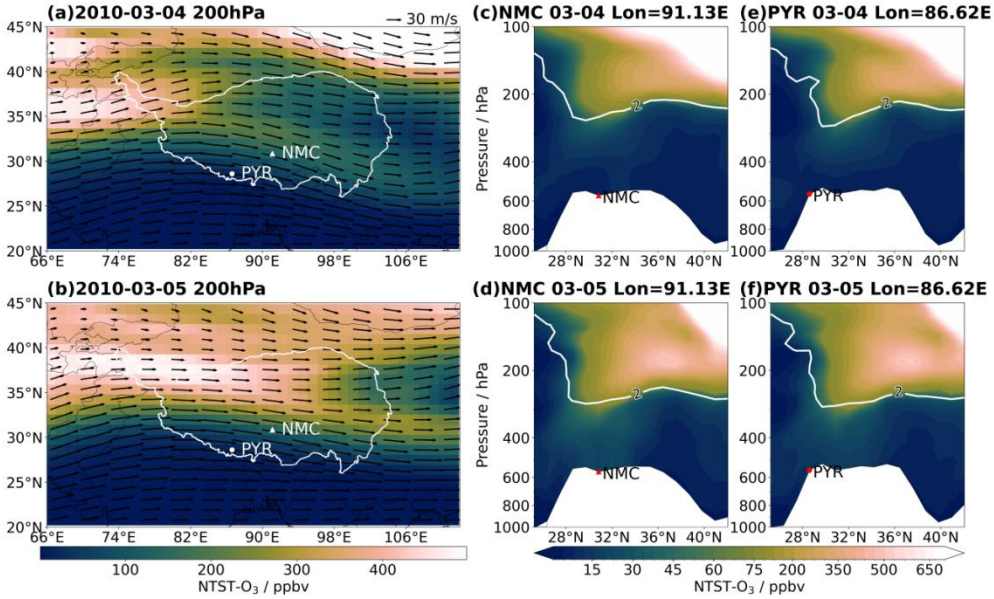

Figure 5. Upper-level tracer distribution and vertical dynamical structure of a stratospheric intrusion event in spring 2010 simulated by the EMAC model: Row 1 (a, c, e) corresponds to 4 March 2010, and Row 2 (b, d, f) corresponds to 5 March 2010. Column 1 (a, b) shows the regional distributions of NTST-O_3 at 200 hPa (color shading) overlaid with wind fields (arrows); White lines highlight the Tibetan Plateau area, and white dots mark the locations of the PYR (circle) and NMC (triangle) stations. Column 2 (c, d) and Column 3 (e, f) present the meridional cross-sections of NMC (Lon=91.13°E) and PYR (Lon=86.62°E), respectively; thick white solid lines denote 2 PVU isopleths, red dots indicate the station locations, and color shading represents NTST-O_3 volume mixing ratio (units: ppbv).

Figures 5c and 5e are the meridional vertical cross-sections of NTST-O_3 mixing ratios at the two stations on 4 March. Above 200 hPa, the high NTST-O_3 mixing ratio center is located over the northern part of the plateau. The NTST-O_3 distribution in the upper atmosphere presents a tongue-like structure sloping southward and extending to the middle troposphere, with the NTST-O_3 mixing ratios above 400 hPa over both stations being higher than 30 ppbv, while the surface NTST-O_3 mixing ratio at the stations is relatively low. A high potential vorticity (PV) tongue (marked by the 2 PVU isopleth) exists in the cross-sections, and it basically overlaps with the distribution of the NTST-O_3 tongue-like structure. The cross-section at NMC shows that the tip of the high PV tongue near the station reaches approximately 260 hPa. The cross-section at PYR shows that the tip of the high PV tongue near the station reaches around 280 hPa. On 4 March, neither the NTST-O_3 tongue tip nor the high PV tongue tip is directly above the stations, with NMC located north of the tongue tips and PYR located south of them.

Figures 5d and 5f are the meridional vertical cross-sections of NTST-O_3 mixing ratios at the two stations on 5 March. It can be observed that a high NTST-O_3 center appears at 200 hPa above the range of 33°N-38°N. The NTST-O_3 distribution in the upper atmosphere has a tongue-like structure sloping southward and extending to lower levels, with the NTST-O_3 mixing

ratio down to 450 hPa over the stations reaching approximately 40 ppbv, and the surface NTST-O_3 mixing ratios at both stations increasing by nearly 5-10 ppbv compared to the previous day. The high PV tongue extends significantly downward compared to the previous day, with the cross-section at NMC showing the tip of the high PV tongue near the station reaching 290 hPa, and the cross-section at PYR showing the tip of the high PV tongue near the station reaching around 300 hPa. Similar to the previous day, neither the NTST-O_3 tongue tip nor the high PV tongue tip is directly above the stations, but both are closer to the stations than on 4 March.

Our analysis of the aforementioned case reveals that the intensification and development of the jet stream promote the transport of stratospheric air masses with high O_3 from the mid-high latitudes north of the Tibetan Plateau down to the central and southern areas above the plateau. The interaction between the jet stream and planetary waves facilitates the occurrence of tropopause folding events, which correspond to the emergence of PV tongues. When the developing high PV tongue, i.e., the deepening of tropopause folding from shallow to deep, is sufficiently close to the stations in both horizontal and vertical dimensions, stratospheric air masses can be effectively mixed into the lower troposphere, leading to the occurrence of stratospheric intrusion events and subsequently resulting in a significant increase in near-surface NTST-O_3.

5.2 Influences of ozone from the tropospheric sources

Figure 6 presents the regional distributions of seasonal mean net photochemical ozone production rates within the planetary boundary layer of Eurasia (30°E-140°E, 0°N-70°N) in different seasons averaged over the period 2010-2012. A stark spatial contrast is evident across all seasons: the Tibetan Plateau primarily acts as a pristine ozone receptor region, whereas its surrounding densely populated and industrialized areas serve as massive regional ozone sources. In spring (Figure 6a), intense net photochemical ozone production is concentrated in South Asia and Southeast Asia with rates commonly exceeding 20 ppbv/day. In contrast, the net production rate over the entire Tibetan Plateau, including the central and southern plateau where NMC and PYR are located, hovers near zero. In summer (Figure 6b), the photochemical ozone production over Eurasia reaches its annual peak, driven by strong solar radiation and abundant precursor emissions. Extensive areas in southern Central Asia, further West Asia and Europe, East Asia and South Asia exhibit prominent production rates exceeding 15 ppbv/day. Strikingly, while the surrounding external sources peak, the Tibetan Plateau acts as a weak chemical sink with negative net production rates (ranging from -1 to 0 ppbv/day), though its eastern and northern peripheries show slightly positive values (1-2 ppbv/day). In autumn (Figure 6c), the net photochemical production in the external source regions begins to decline, but South Asia and southern China remain active sources. In winter (Figure 6d), the high net production belt retreats to lower latitudes (South and Southeast Asia), and the boundary layer over the plateau acts predominantly as a weak sink. This persistent absence of local net photochemical generation confirms that surface ozone over the plateau is overwhelmingly transported from external source regions.~~value production belt retreats to lower latitudes (South and Southeast Asia), and the boundary layer over the plateau acts predominantly as a weak sink. This persistent absence of local photochemical generation confirms that the surface ozone concentrations over the plateau are overwhelmingly governed by long-range transport from external source regions.~~

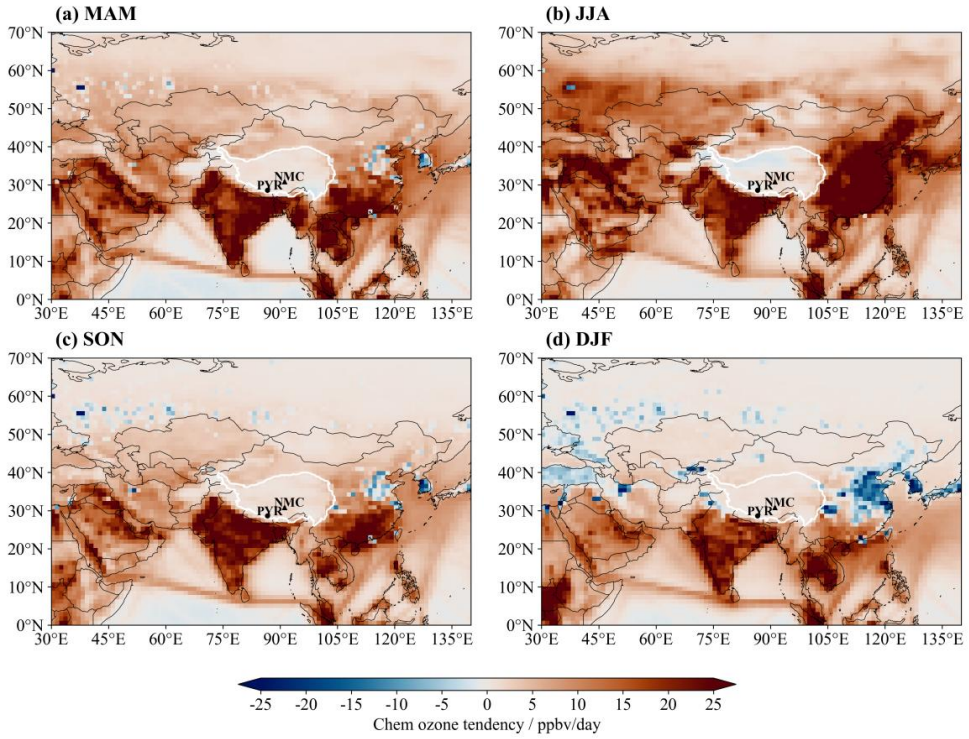

Figure 6. EMAC simulated regional distributions of net photochemical ozone production rates within the planetary boundary layer over parts of Eurasia (35°E-125°E, 20°N-70°N) in different seasons averaged over the period 2010-2012: (a) Spring, (b) Summer, (c) Autumn, (d) Winter. Color shading denotes the net photochemical ozone production rate (units: ppbv/day). White lines highlight the Tibetan Plateau area, and black dots mark the locations of the PYR (circle) and NMC (triangle) stations.

5.2.1 Seasonal patterns of surface ozone from the tropospheric sources

Strong convective activity and updrafts can lift boundary-layer ozone and its precursors into the mid-troposphere over the source and pollution-plume areas. Once lofted to the mid-troposphere, these ozone-rich air masses are captured by large-scale circulation systems at mid-to-high latitudes and then horizontally advected toward the Tibetan Plateau by broad "steering winds", as shown in the 500 hPa wind fields in Figure 7. Upon encountering the massive topography of the plateau, large-scale subsidence and terrain-following downdrafts ultimately transport ozone generated from external source regions down to the surface layer of the Tibetan Plateau.

Figure 7 presents the regional distributions of surface NHTS-O_3 and 500 hPa mean wind field over parts of Eurasia (35°E-125°E, 20°N-70°N) in different seasons averaged over the period 2010-2012. The relative contributions of NHTS-O_3 to total surface ozone are shown correspondingly in Figure S97 in the Supplement. The NHTS-O_3 high-value belt is concentrated in the north-central Eurasian region between 30°N and 50°N, and its impact on surface O_3 over the Tibetan

Plateau is mutually regulated by source-region concentrations and the 500 hPa westerly circulation. In spring (Figure 7a), surface NHTS-O_3 mixing ratios over Eurasia are relatively low, typically below 40 ppbv. Influenced by the split circulation of the westerly belt, strong northwest winds dominate the northern Tibetan Plateau. At the northern edge of the plateau (35°N-40°N) surface NHTS-O_3 mixing ratios reach 25-32 ppbv, larger than those of the central and southern plateau where NMC and PYR are located. In summer (Figure 7b), surface NHTS-O_3 mixing ratios over Eurasia are largest annually, with several prominent NHTS-O_3 sources (mixing ratios exceeding 55 ppbv) located in the upstream regions of the Tibetan Plateau. During this season, the zonal circulation transports NHTS-O_3 from these external source areas, including southern Central Asia and further West Asia and Europe, to the plateau, resulting in an annual maximum of surface NHTS-O_3 mixing ratios in the northern plateau (reaching 40-50 ppbv). The southern plateau, where PYR is located, is relatively less affected by transport of NHTS-O_3 from these source regions compared to the central plateau, where NMC is located. In autumn (Figure 7c), NHTS-O_3 in the aforementioned external sources appears to decrease, and the transport effects on surface O_3 over the plateau decrease. In winter (Figure 7d), surface NHTS-O_3 mixing ratios over Eurasia are generally below 25 ppbv, and those over the plateau drop to their annual minimum.

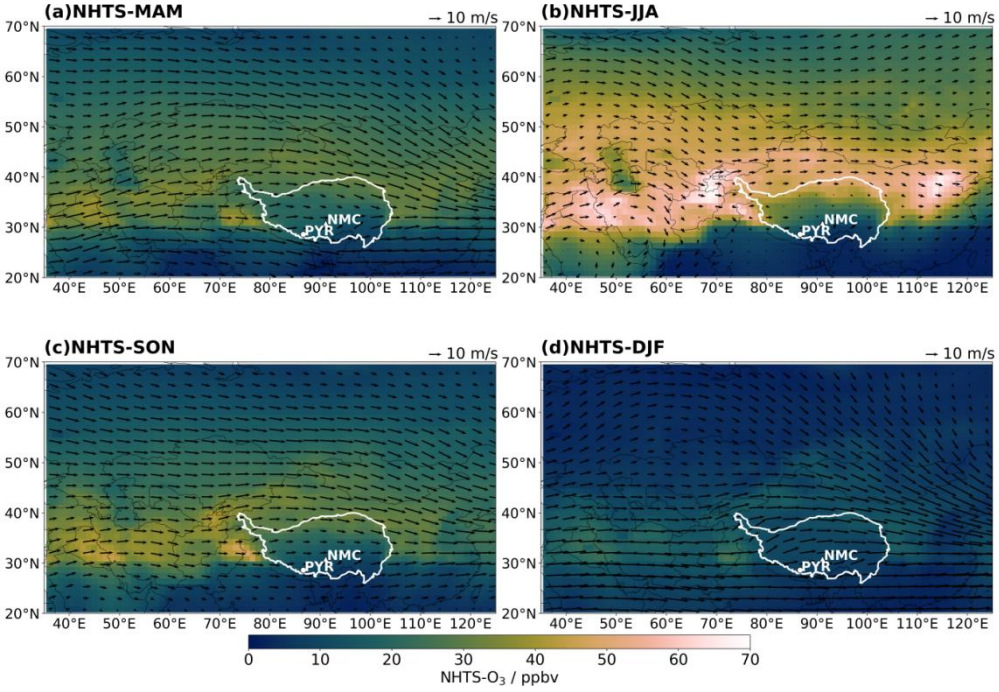

Figure 7. EMAC simulated regional distributions of surface NHTS-O_3 and 500 hPa wind field over parts of Eurasia (35°E-125°E, 20°N-70°N) in different seasons averaged over the period 2010-2012: (a) Spring, (b) Summer, (c) Autumn, (d) Winter. Color shading denotes NHTS-O_3 volume mixing ratio (units: ppbv), and black arrows represent the wind field (units: m/s). White lines highlight the Tibetan Plateau area, and white dots mark the locations of the PYR (circle) and NMC (triangle) stations.

Figure 8 presents the regional distributions of surface TRTS-O_3 and boundary layer mean wind field over a larger Tibetan Plateau, South Asia, and Southeast Asia area in different seasons, averaged over the period 2010-2012. For reference, the corresponding relative contributions of TRTS-O_3 to total modelled O_3 are presented in Figure S8 in the Supplement. TRTS-O_3 mixing ratios reach their annual maximum in spring (Figure 8a). During this season, frequent crop residue burning after harvest and wildfires occur in South Asia and Southeast Asia (Xue et al., 2020), leading to strong emissions of O_3 precursors in this region (Lalitaporn, 2018; Lalitaporn and Boonmee, 2019) and subsequent substantial O_3 production via photochemical reactions (Li et al., 2025; Sukkhum et al., 2022; Yang et al., 2022). Consequently, TRTS-O_3 mixing ratios exceed 60 ppbv in northeastern South Asia and northern Southeast Asia, and the air masses with high TRTS-O_3 can be transported to the southern Tibetan Plateau by southwesterly airflows, resulting in a spatial pattern where surface TRTS-O_3 mixing ratios decrease progressively from the southern to the northern parts of the plateau, with larger impacts on PYR than on NMC. Surface TRTS-O_3 mixing ratios over the southern plateau (26°N-30°N) range from 45 to 60 ppbv. With the northward advance of the Asian summer monsoon, the summer boundary layer wind field (Figure 8b) shows that South and Southeast Asia are strongly influenced by southwesterly winds. Abundant water vapor (through $O(^1D) + H_2O$) and frequent precipitation reduce O_3 production in South Asia and Southeast Asia (Gao et al., 2020; Lu et al., 2018; Wang et al., 2022), causing TRTS-O_3 to drop to its annual minimum. Surface TRTS-O_3 mixing ratios in the southern plateau range from 30 to 40 ppbv, decreasing progressively from the south to the north. In autumn (Figure 8c), the monsoon retreats southward, accompanied by reduced precipitation and weakened convection. This leads to increased O_3 production in South and Southeast Asia, and a subsequent rise in surface TRTS-O_3 mixing ratios over the Tibetan Plateau. In winter (Figure 8d), increased fire activity leads to a sharp rise in O_3 production in South Asia (Yang et al., 2022). However, surface TRTS-O_3 over the Tibetan Plateau does not increase so significantly as expected from its source variations, due to the wind fields in this season that are unfavorable for the transport of air masses to the plateau.

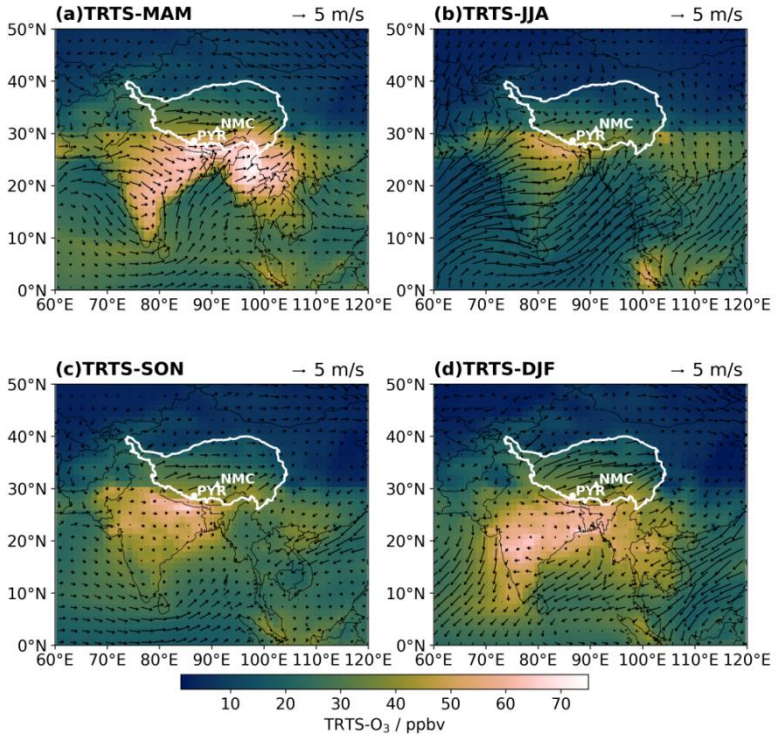

Figure 8. EMAC simulated regional distributions of surface TRTS-O_3 and boundary layer average wind field over a larger area covering the Tibetan Plateau, South Asia, and Southeast Asia in different seasons averaged over the period 2010–2012: (a) Spring, (b) Summer, (c) Autumn, (d) Winter. Color shading denotes TRTS-O_3 volume mixing ratio (units: ppbv), and black arrows represent the wind field (units: m/s). White lines highlight the Tibetan Plateau area, and white dots mark the locations of the PYR (circle) and NMC (triangle) stations.

5.2.2 Surface ozone from the tropospheric sources at different monsoon phases

The Asian summer monsoon has a large impact on the changes of surface ozone over the Tibetan Plateau (Ma et al., 2022). Here, we further investigate variations of surface NHTS-O_3 and TRTS-O_3 over the Tibetan Plateau during different monsoon phases, using 2012 as an example. Figure 9 presents the time series of daily surface NHTS-O_3, TRTS-O_3, specific humidity (q_v), and precipitation at 88.88°E (the midpoint of the longitudes of NMC and PYR, spanning the zonal extent of the Tibetan Plateau) at different latitudes throughout 2012. The relative contributions of tagged O_3 from these two sources to total modeled ozone along the same cross-section are detailed in Figure S9 in the Supplement. Specific humidity and precipitation data are also analyzed here, considering that their variations are useful indicators for different monsoon phases (Figures 9c, d). Figure 89a shows that, within the Tibetan Plateau domain, the NHTS-O_3 mixing ratio high-value belt is stably distributed north of 35°N. NHTS-O_3 mixing ratios in this high-value belt reach their annual maximum (exceeding 60 ppbv) in June-August. The figure shows that within the NHTS domain (the region north of 29.3°N, marked by the black

dashed line), the summer monsoon has negligible influence; the distribution of NHTS-O_3 is only regulated by the seasonal variation of source-region concentrations and mid-high latitude circulation. In contrast, from 29.3°N to the southern boundary of the Tibetan Plateau (marked by the thick black dashed line), NHTS-O_3 mixing ratios remain low during the summer monsoon period, due to weakened transport and precipitation scavenging. Figure 9b shows that the distribution of TRTS-O_3 mixing ratios exhibits a distinct spatial pattern of progressive decrease from the southern boundary of the plateau to its northern part, directly reflecting the transport attenuation pattern of TRTS-O_3 to the Tibetan Plateau. During the pre-monsoon period, TRTS-O_3 mixing ratios south of 29.3°N reach their annual peak (exceeding 60 ppbv in some periods). There is strong transport of TRTS-O_3 from the southern boundary of the plateau to its northern interior, with TRTS-O_3 mixing ratios near 33°N reaching 45 ppbv. During the monsoon period, TRTS-O_3 mixing ratios south of 29.3°N decrease significantly. Meanwhile, specific humidity and precipitation in this region increase synchronously. This suppresses TRTS-O_3 production in the source regions, thereby leading to lower TRTS-O_3 mixing ratios over the plateau. During the post-monsoon period, the monsoon exerts less influence on the source regions, and TRTS-O_3 mixing ratios rebound. This process clearly demonstrates the regulatory effect of the monsoon on the production of O_3 in the TRTS source regions directly, and its subsequent impact on surface O_3 levels over the plateau through the transport.

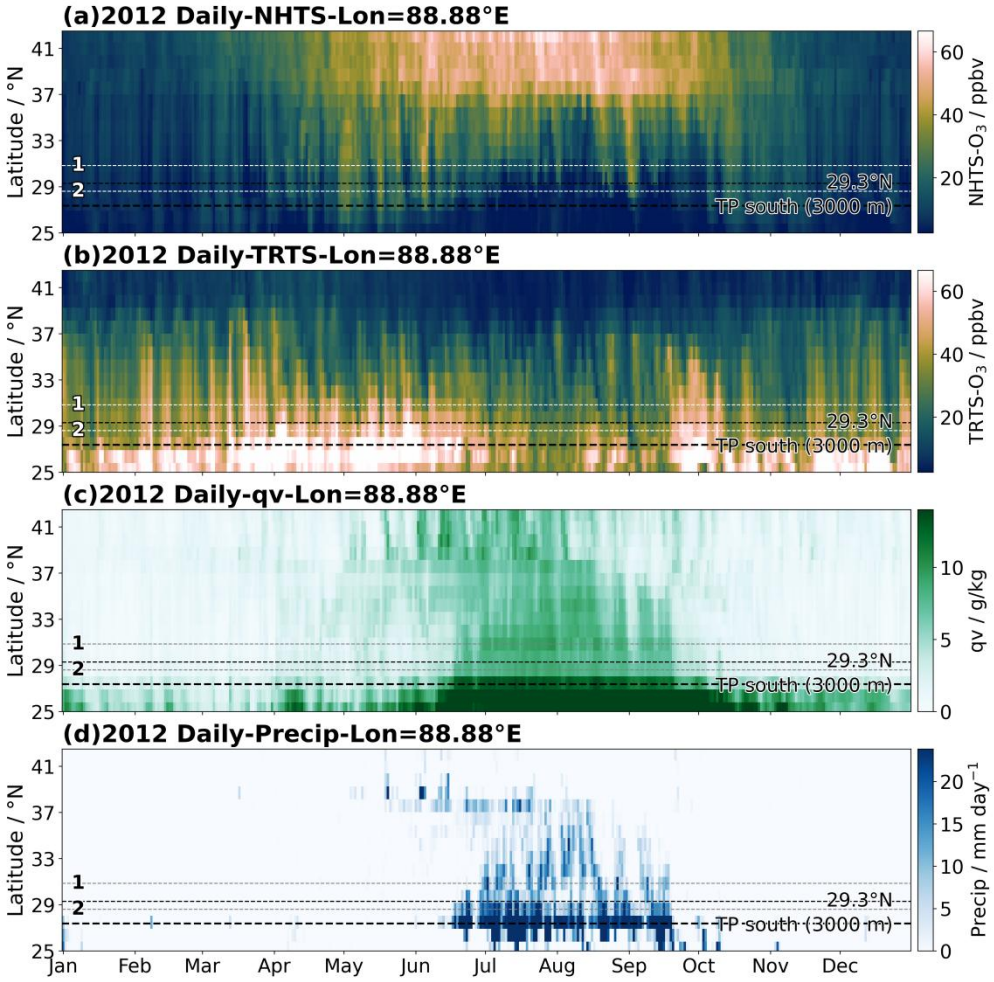

Figure 9. Time series of daily average surface (a) NHTS-O_3 mixing ratio (units: ppbv), (b) TRTS-O_3 mixing ratio (units: ppbv), (c) specific humidity (qv, units: g kg^{-1}), and (d) precipitation (units: mm day^{-1}) over the Tibetan Plateau at 88.88°E longitude (the midpoint of the longitudes of the two stations, NMC and PYR) in 2012, simulated by the EMAC model. The latitude 29.3°N (the boundary between the NHTS and TRTS source regions) is marked by a black dashed line, and dashed gray lines with numbered labels indicate the latitudes of the two stations (with "1" for NMC and "2" for PYR). The thick black dashed line indicates the southern boundary of the Tibetan Plateau at this longitude.

5.2.3 Analysis of tropospheric ozone transport events

Based on the interdaily variability of surface NHTS-O_3 at the two stations presented in Sect. 4.2, we selected a typical event of strong NHTS-O_3 transport to the central and southern Tibetan Plateau, which occurred from 3 to 4 June 2012, for in-depth analysis. Figure 10 presents the regional distributions of surface NHTS-O_3 and boundary layer mean wind field over

the Tibetan Plateau on 3 and 4 June 2012. The spatial patterns of the relative contribution of NHTS-O_3 to total modelled O_3 during this episode are provided in Figure S120 in the Supplement. This episode corresponds to a predominant-contribution period (above the 95th percentile) for NHTS-O_3 on the southern plateau. Figure 10a shows that a high-mixing ratio center of NHTS-O_3 (exceeding 50 ppbv) existed over the western area adjacent to the Tibetan Plateau (75°E-85°E, 30°N-34°N) on 3 June. The surface NHTS-O_3 mixing ratio was 19 ppbv at NMC and was 21 ppbv at PYR. The boundary layer mean wind field indicates strong westerly winds over the western Tibetan Plateau, with southwest winds prevailing at both PYR and NMC. Driven by the strong westerly winds transporting high-concentration NHTS-O_3 from the western plateau to its central part, the high-value center of NHTS-O_3 (>50 ppbv) over the Tibetan Plateau shifted eastward to 89°E on 4 June (Figure 10b). Surface NHTS-O_3 mixing ratios over the plateau increased significantly compared to the previous day, to build up by 36 ppbv at NMC and 43 ppbv at PYR. This event demonstrates that intense transport processes can deliver high-concentration NHTS-O_3 from outside the plateau into its central and southern regions, causing a rapid increase in surface NHTS-O_3 mixing ratios in these areas. A similar event occurring from 4 to 5 June 2011 is shown in Figure S142.

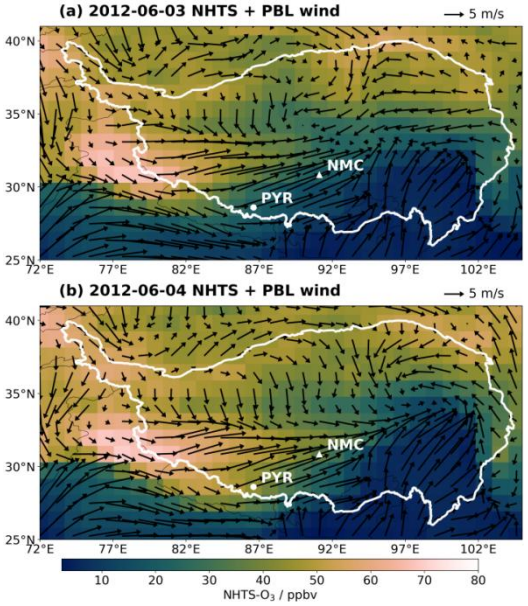

Figure 10. EMAC simulated changes in the regional distribution of surface NHTS-O_3 (color shading, units: ppbv) and the boundary layer average wind field (arrows, units: m/s) during a typical NHTS-O_3 transport event over the Tibetan Plateau: (a) corresponds to 3 June 2012, and (b) corresponds to 4 June 2012. White lines highlight the Tibetan Plateau area, and white dots mark the locations of the PYR (circle) and NMC (triangle) stations.

To examine the interdaily variation characteristics of surface TRTS-O_3 at the two stations during the monsoon period, we selected a typical event of strong TRTS-O_3 transport to the central and southern Tibetan Plateau, occurring from 8 to 9 August 2012, for in-depth analysis (Figure 11). The relative contribution of TRTS-O_3 during this transport event is presented in Figure S11 in the Supplement to contextualize its impact. This episode corresponds to a predominant -contribution period

(above the 95th percentile) for TRTS-O_3 at the southern plateau. On 8 August (Figure 11a), a strong precipitation belt existed in the central (82°E-93°E, 33°N–37°N) and southwestern (78°E-93°E, 26°N-32°N) Tibetan Plateau, with the daily accumulated precipitation reaching 5 mm/day at NMC and 17 mm/day at PYR. The boundary layer average wind field shows a low-level vortex structure in the central and southern Tibetan Plateau (west of NMC, north of PYR), while the wind direction was weak westerly at PYR and strong southerly at NMC. On 8 August (Figure 11b), surface TRTS-O_3 mixing ratios in the southern Tibetan Plateau (25°N-30°N) ranged from 20 to 40 ppbv, with 22 ppbv at NMC and 36 ppbv at PYR. For the boundary layer wind field on 9 August (Figure 11c), the low-level vortex observed on the previous day moved westward to the northwestern Tibetan Plateau, and strong southerly winds prevailed at both NMC and PYR. Precipitation at NMC disappeared, while the daily accumulated precipitation at PYR decreased to 8 mm/day. Due to the strong and dry low-level southerly winds and weakened wet deposition caused by reduced precipitation, surface TRTS-O_3 in the central and southern Tibetan Plateau increased significantly on 9 August compared to the previous day, rising to 39 ppbv at PYR and 31 ppbv at NMC (Figure 11d). This event indicates that during the monsoon period, surface TRTS-O_3 on the central and southern Tibetan Plateau can change rapidly from day to day with variations in atmospheric circulation and precipitation. A similar event occurring from 6 to 7 June 2012 is shown in Figure S153.

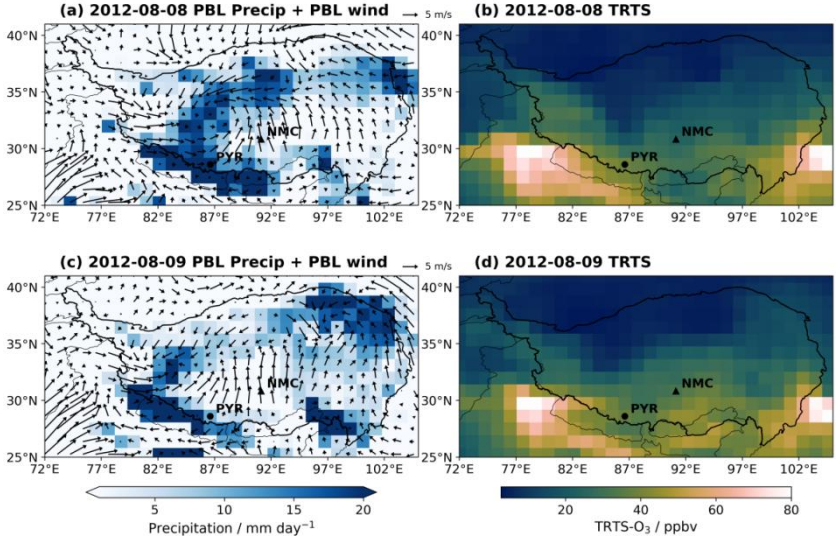

Figure 11. EMAC simulated changes in the regional distribution of surface TRTS-O_3 for a typical TRTS-O_3 transport event during the 2012 Asian summer monsoon: Row 1 (a, b) corresponds to 8 August 2012, and Row 2 (c, d) corresponds to 9 August 2012. Column 1 (a, c) shows the regional distributions of daily accumulated precipitation (color shading, units: mm day^{-1}) overlaid with the boundary layer average wind field (arrows, units: m/s). Column 2 (b, d) presents the regional distributions of surface TRTS-O_3 (units: ppbv). Black lines highlight the Tibetan Plateau area, and black dots mark the locations of the PYR (circle) and NMC (triangle) stations.

6 Conclusions

Based on a comprehensive analysis of in-situ observational data and EMAC model simulations of ozone tagged for different stratospheric and tropospheric regions, this study systematically revealeds the sources and spatiotemporal distribution characteristics of surface O_3 at the NMC and PYR stations and in the surrounding areas of the Tibetan Plateau. The main conclusions are as follows:

The EMAC model can reproduce the seasonal and synoptic-scale variation and tendencies of surface O_3 at the two stations in the central and southern Tibetan Plateau, but exhibits significant differences in simulation accuracy between the two stations. For the NMC station in the central plateau, the model shows high simulation accuracy with an MB of 3.2 ppbv and an RMSE of 10.9 ppbv for daily surface O_3 mixing ratios. However, the model exhibits a systematic overestimation at the PYR station over the southern plateau, with an MB of 12.6 ppbv and an RMSE of 16.1 ppbv. This discrepancy mainly reflects the difficulty of representing the steep and highly heterogeneous terrain, the complex underlying surface conditions, and the associated local transport processes over the southern Tibetan Plateau at the current model resolution. The positive bias is most pronounced during late spring and early summer, when stratospheric influence and photochemical O_3 formation are both strong, but this does not necessarily imply a unique overestimation of any single tagged source. Instead, we interpret the PYR bias as a model limitation that affects the absolute magnitudes of surface O_3, while the simulated seasonal cycles and relative source contributions remain physically meaningful and robust within the current model configuration. Therefore, we interpret the source-attribution results at PYR as physically meaningful representations of regional-scale transport within the current model configuration, while noting that their absolute values are subject to local topographical uncertainties. ~~This discrepancy reflects that the model's ability to simulate the complex underlying surface conditions, topographic effects, and local processes in the southern Tibetan Plateau needs further improvement. The overestimated ozone at the surface occurred during periods of maximum transport from the stratosphere and photochemical O_3 formation (late spring/early summer), leaving the impression that both sources may be overestimated to some degree.~~

This study has analyzed the spatiotemporal variability of O_3 over the Tibetan Plateau transported from the three source regions, namely the Northern Hemisphere and Tropical Stratospheric Source (NTST), the Northern Hemisphere Mid-High Latitude Tropospheric Source (NHTS), and the Tropical Tropospheric Source (TRTS), which are treated by EMAC using the ozone source tagging technique. Surface NTST-O_3 is highest in spring annually at both stations (with a maximum daily average mixing ratio of 28 ppbv at NMC and 22 ppbv at PYR). It exhibits a strong interdaily variability during springtime stratospheric intrusion events, with a maximum interdaily difference of 15 ppbv at NMC and 11 ppbv at PYR. Surface NHTS-O_3 is highest in summer, with a maximum daily average mixing ratio of 40 ppbv at NMC and 45 ppbv at PYR, and it also exhibits an intense interdaily variability, with a maximum of 22 ppbv at both stations. Surface TRTS-O_3 is highest during spring, especially during the pre-monsoon period, and it exhibits a spatial pattern of being higher in the south and lower in the north over the Tibetan Plateau, with a maximum daily average mixing ratio of 77 ppbvat PYR and 64 ppbv at NMC.

The seasonal and daily variations of NTST-O_3 over the Tibetan Plateau are primarily regulated by the changes in the position and intensity of the subtropical westerly jet. In spring, the jet axis is located in the hinterland of the plateau, and its interaction with planetary waves induces frequent tropopause folding events, which promote the downward transport of stratospheric O_3 to the troposphere, leading to the spring peak and strong interdaily variability of NTST-O_3 at the surface. The relative contribution of NTST-O_3 to surface O_3 can reach a daily maximum of 30% at both NMC and PYR. Surface NHTS-O_3 on the Tibetan Plateau is mutually regulated by variations in NHTS-O_3 concentrations in the source regions and the westerly circulation indicated by the 500 hPa wind field. Since surface NHTS-O_3 in Central Asia, West Asia and Europe are highest in summer, efficient transport of NHTS-O_3 by zonal circulation from these source regions results in a summertime maximum of surface O_3 over the northern plateau. The relative contribution of NHTS-O_3 to surface O_3 can reach a daily maximum of 62% at NMC and 58% at PYR in summer, although the absolute contributions are relatively small due to limited southward transport of NHTS-O_3 over the plateau.

Surface TRTS-O_3 over the Tibetan Plateau is controlled by the TRTS-O_3 concentrations in the South and Southeast Asian source areas and monsoon circulation. In addition to biomass burning activities, the Asian summer monsoon regulates surface TRTS-O_3 by modifying the environmental conditions, such as total water content and precipitation in the tropical source regions. During the pre-monsoon period, enhanced TRTS-O_3 in South and Southeast Asia can be transported to the plateau, resulting in annual surface O_3 peaks over the southern and central Tibetan Plateau. The relative contribution of TRTS-O_3 to surface O_3 can reach a daily maximum of 93% at NMC and 98% at PYR in this period. During the monsoon period, O_3 production is suppressed in the source regions, and transport of TRTS-O_3 to the plateau is limited, leading to annual minimums of surface TRTS-O_3 over the southern and central Tibetan Plateau, as observed at NMC and PYR. During monsoon breaks, when precipitation weakens, and TRTS-O_3 concentrations increase in the source regions, short-term TRTS-O_3 enhancement events can occur over the central and southern plateau under favorable transport conditions.

By analyzing ozone variations across multiple spatial and temporal scales~~Through multi-scale analsis~~, this study elucidates the key roles of monsoon and zonal~~westerly~~ circulation as well as subtropical westerly jet in the dynamics and transport of O_3 from the TRTS, NHTS and NTST source regions to the Tibetan Plateau. Although several areas, including South, Southeast, Central and West Asia, and further Europe, have been identified as major sources of surface O_3 over the Tibetan Plateau, additional studies, including model simulation are needed to quantify the contributions of these important sources to the seasonal and daily variations of O_3 over the Tibetan Plateau. Additional measurements, especially in the western, southwestern and northwestern parts of the plateau, are suggested to evaluate and improve the model simulations and reveal the sources and transport pathways of O_3 to the plateau. It should be noted that the present analysis is limited to the observationally available period of 2010 – 2012. According to historical sea surface temperature data, this period was characterized by persistent La Niña conditions (Feng et al., 2015). Previous studies have shown that the El Niño-Southern Oscillation (ENSO) and the stratospheric quasi-biennial oscillation (QBO) can strongly influence cross-tropopause transport and tropospheric ozone anomalies (Han et al., 2001; Li et al., 2023; Li et al., 2024), while the 11-year solar cycle contributes to longer-term ozone variations (Xu et al., 2016; Xu et al., 2018a). Future studies employing long-term transient simulations

are essential to quantify the impacts of these climate modes on the interannual variability of ozone sources over the TP. Spatiotemporal variations of O_3 over the Tibetan Plateau, as well as associated influencing factors, are complex, and with ongoing changes in the emissions of ozone precursors in the major source areas and enhanced climate variabilities, the influences on surface O_3 over the Tibetan Plateau through transport and photochemistry need continued investigation.

Data availability. Ozone measurements from NMC can be made available on request. The ozone dataset of PYR used in this study were accessed from EBAS (https://ebas.nilu.no; DOI: https://doi.org/10.48597/ASM8-VJYZ) hosted by NILU and affiliated with the GAW-WDCRG framework. The data were accessed on 12 November 2024 and comprise hourly ozone mixing ratios for 2010-2012. The usage of MESSy (Modular Earth Submodel System) and access to the source code is licensed to all affiliates of institutions which are members of the MESSy Consortium. Institutions can become members of the MESSy Consortium by signing the "MESSy Memorandum of Understanding". More information can be found on the MESSy Consortium website: http://www.messy-interface.org (last access: 3 November 2025). The code used in this study has been based on MESSy version 2.52. The data produced in the study are available from the authors upon request.

Supplement. The supplement related to this article is available online.

Author contributions. YZ analysed the data under discussion with JM. JM performed the model simulation. NL, AP, and JL contributed to the model simulation and evaluation. WL and XX made measurements at NMC. YL, SC, and XZ contributed to data processing and the analysis, YZ and JM prepared the manuscript with contributions from all co-authors.

Competing interests. At least one of the (co-)authors is a member of the editorial board of Atmospheric Chemistry and Physics.

Special issue statement. This article is part of the special issue " The Modular Earth Submodel System (MESSy) (ACP/GMD inter-journal SI)". It is not associated with a conference.

Acknowledgements. JM would like to thank Patrick Jöckel, Rolf Sander, and other MESSy colleagues for their help in using EMAC and the submodels. Hualong Zhang, Shihui Jia and Ying Wang participated in the observations at NMC.

Financial support. This research has been supported by the National Natural Science Foundation of China (grant nos. 42330603, 42475123) and the CAMS Science and Technology Development Fund (grant no. 2023KJ013).

References

Archibald, A. T., Neu, J. L., Elshorbany, Y. F., Cooper, O. R., Young, P. J., Akiyoshi, H., Cox, R. A., Coyle, M., Derwent, R. G., Deushi, M., Finco, A., Frost, G. J., Galbally, I. E., Gerosa, G., Granier, C., Griffiths, P. T., Hossaini, R., Hu, L., Joeckel, P., Josse, B., Lin, M. Y., Mertens, M., Morgenstern, O., Naja, M., Naik, V., Oltmans, S., Plummer, D. A., Revell, L. E., Saiz-Lopez, A., Saxena, P., Shin, Y. M., Shahid, I., Shallcross, D., Tilmes, S., Trickl, T., Wallington, T. J., Wang, T., Worden, H. M., and Zeng, G.: Tropospheric Ozone Assessment Report: A critical review of changes in the tropospheric ozone burden and budget from 1850 to 2100, Elem. Sci. Anth., https://doi.org/10.1525/elementa.2020.034, 2020.

Bonasoni, P., Laj, P., Angelini, F., Arduini, J., Bonafè, U., Calzolari, F., Cristofanelli, P., Decesari, S., Facchini, M. C., Fuzzi, S., Gobbi, G. P., Maione, M., Marinoni, A., Petzold, A., Roccato, F., Roger, J. C., Sellegri, K., Sprenger, M., Venzac, H., Verza, G. P., Villani, P., and Vuillermoz, E.: The ABC-Pyramid Atmospheric Research Observatory in Himalaya for aerosol, ozone and halocarbon measurements, Sci. Total Environ., 391, 252-261, https://doi.org/10.1016/j.scitotenv.2007.10.024, 2008.

Bonasoni, P., Laj, P., Marinoni, A., Sprenger, M., Angelini, F., Arduini, J., Bonafè, U., Calzolari, F., Colombo, T., Decesari, S., Di Biagio, C., di Sarra, A. G., Evangelisti, F., Duchi, R., Facchini, M. C., Fuzzi, S., Gobbi, G. P., Maione, M., Panday, A., Roccato, F., Sellegri, K., Venzac, H., Verza, G. P., Villani, P., Vuillermoz, E., and Cristofanelli, P.: Atmospheric Brown Clouds in the Himalayas: first two years of continuous observations at the Nepal Climate Observatory-Pyramid (5079 m), Atmos. Chem. Phys., 10, 7515-7531, https://doi.org/10.5194/acp-10-7515-2010, 2010.

Chen, X. L., Ma, Y. M., Kelder, H., Su, Z., and Yang, K.: On the behaviour of the tropopause folding events over the Tibetan Plateau, Atmos. Chem. Phys., 11, 5113-5122, https://doi.org/10.5194/acp-11-5113-2011, 2011.

Cristofanelli, P., Bonasoni, P., Collins, W., Feichter, J., Forster, C., James, P., Kentarchos, A., Kubik, P. W., Land, C., Meloen, J., Roelofs, G. J., Siegmund, P., Sprenger, M., Schnabel, C., Stohl, A., Tobler, L., Tositti, L., Trickl, T., and Zanis, P.: Stratosphere-to-troposphere transport: A model and method evaluation, J. Geophys. Res.-Atmos., 108, 8525, https://doi.org/10.1029/2002JD002600, 2003.

Cristofanelli, P., Bracci, A., Sprenger, M., Marinoni, A., Bonafè, U., Calzolari, F., Duchi, R., Laj, P., Pichon, J. M., Roccato, F., Venzac, H., Vuillermoz, E., and Bonasoni, P.: Tropospheric ozone variations at the Nepal Climate Observatory-Pyramid (Himalayas, 5079 m a.s.l.) and influence of deep stratospheric intrusion events, Atmos. Chem. Phys., 10, 6537-6549, https://doi.org/10.5194/acp-10-6537-2010, 2010.

Desqueyroux, H., Pujet, J.-C., Prosper, M., Squinazi, F., and Momas, I.: Short-Term Effects of Low-Level Air Pollution on Respiratory Health of Adults Suffering from Moderate to Severe Asthma, Environ. Res., 89, 29-37, https://doi.org/10.1006/enrs.2002.4357, 2002.

Ding, A. and Wang, T.: Influence of stratosphere-to-troposphere exchange on the seasonal cycle of surface ozone at Mount Waliguan in western China, Geophys. Res. Lett., 33, L03803, https://doi.org/10.1029/2005GL024760, 2006.

Eckstein, J., Ruhnke, R., Zahn, A., Neumaier, M., Kirner, O., and Braesicke, P.: An assessment of the climatological representativeness of IAGOS-CARIBIC trace gas measurements using EMAC model simulations, Atmos. Chem. Phys., 17, 2775-2794, https://doi.org/10.5194/acp-17-2775-2017, 2017.

Feng, L., Zhang, R.-H., Wang, Z., and Chen, X.: Processes leading to second-year cooling of the 2010–12 La Niña event, diagnosed using GODAS, Adv. Atmos. Sci., 32, 424-438, https://doi.org/10.1007/s00376-014-4012-8, 2015.

Gao, M., Gao, J., Zhu, B., Kumar, R., Lu, X., Song, S., Zhang, Y., Jia, B., Wang, P., Beig, G., Hu, J., Ying, Q., Zhang, H., Sherman, P., and McElroy, M. B.: Ozone pollution over China and India: seasonality and sources, Atmos. Chem. Phys., 20, 4399-4414, https://doi.org/10.5194/acp-20-4399-2020, 2020.

Granier, C., Bessagnet, B., Bond, T. C., D'Angiola, A., Denier van der Gon, H. A. C., Frost, G. J., Heil, A., Kaiser, J. W., Kinne, S., Klimont, Z., Kloster, S., Lamarque, J. F., Liousse, C., Masui, T., Meleux, F., Mieville, A., Ohara, T., Raut,

J.-C., Riahi, K., Schultz, M. G., Smith, S. J., Thompson, A., Aardenne, J. A. v., Werf, G. R., and Vuuren, D. v.: Evolution of anthropogenic and biomass burning emissions of air pollutants at global and regional scales during the 1980–2010 period, Climatic Change, 109, 163-190, https://doi.org/10.1007/s10584-011-0154-1, 2011.

Grewe, V.: The origin of ozone, Atmos. Chem. Phys., 6, 1495-1511, https://doi.org/10.5194/acp-6-1495-2006, 2006.

Guerova, G., Bey, I., Attié, J. L., Martin, R. V., Cui, J., and Sprenger, M.: Impact of transatlantic transport episodes on summertime ozone in Europe, Atmos. Chem. Phys., 6, 2057-2072, https://doi.org/10.5194/acp-6-2057-2006, 2006.

Han, Z., Chongping, J., Libo, Z., Wei, W., and Yongxiao, J.: ENSO signal in total ozone over Tibet, Adv. Atmos. Sci., 18, 231-238, https://doi.org/10.1007/s00376-001-0016-2, 2001.

Hayashida, S., Kajino, M., Deushi, M., Sekiyama, T. T., and Liu, X.: Seasonality of the lower tropospheric ozone over China observed by the Ozone Monitoring Instrument, Atmos. Environ., 184, 244-253, https://doi.org/10.1016/j.atmosenv.2018.04.014, 2018.

Holton, J. R., Haynes, P. H., McIntyre, M. E., Douglass, A. R., Rood, R. B., and Pfister, L.: Stratosphere-troposphere exchange, Rev. Geophys., 33, 403-439, https://doi.org/10.1029/95RG02097, 1995.

Hough, A. M. and Derwent, R. G.: Changes in the global concentration of tropospheric ozone due to human activities, Nature, 344, 645-648, https://doi.org/10.1038/344645a0, 1990.

Jacob, D. J., Logan, J. A., and Murti, P. P.: Effect of rising Asian emissions on surface ozone in the United States, Geophys. Res. Lett., 26, 2175-2178, https://doi.org/10.1029/1999GL900450, 1999.

James, P., Stohl, A., Forster, C., Eckhardt, S., Seibert, P., and Frank, A.: A 15-year climatology of stratosphere-troposphere exchange with a Lagrangian particle dispersion model: 1. Methodology and validation, J. Geophys. Res.-Atmos., 108, 8519, https://doi.org/10.1029/2002JD002637, 2003.

Jöckel, P., Sander, R., Kerkweg, A., Tost, H., and J., L.: Technical Note: The Modular Earth Submodel System (MESSy) - a new approach towards Earth System Modeling, Atmos. Chem. Phys., 5, 433-444, https://doi.org/10.5194/acp-5-433-2005, 2005.

Jöckel, P., Tost, H., Pozzer, A., Brühl, C., Buchholz, J., Ganzeveld, L., Hoor, P., Kerkweg, A., G., L. M., R., S., B., S., G., S., M., T., D., T., J., v. A., and J., L.: The atmospheric chemistry general circulation model ECHAM5/MESSy1: consistent simulation of ozone from the surface to the mesosphere, Atmos. Chem. Phys., 6, 5067-5104, https://doi.org/10.5194/acp-6-5067-2006, 2006.

Jöckel, P., Kerkweg, A., Pozzer, A., Sander, R., Tost, H., Riede, H., Baumgaertner, A., Gromov, S., and Kern, B.: Development cycle 2 of the Modular Earth Submodel System (MESSy2), Geosci. Model Dev., 3, 717-752, https://doi.org/10.5194/gmd-3-717-2010, 2010.

Jöckel, P., Tost, H., Pozzer, A., Kunze, M., Kirner, O., Brenninkmeijer, C. A. M., Brinkop, S., Cai, D. S., Dyroff, C., Eckstein, J., Frank, F., Garny, H., Gottschaldt, K.-D., Graf, P., Grewe, V., Kerkweg, A., Kern, B., Matthes, S., Mertens, M., Meul, S., Neumaier, M., Nützel, M., Oberländer-Hayn, S., Ruhnke, R., Runde, T., Sander, R., Scharffe, D., and Zahn, A.: Earth System Chemistry integrated Modelling (ESCiMo) with the Modular Earth Submodel System (MESSy) version 2.51, Geosci. Model Dev., 9, 1153-1200, https://doi.org/10.5194/gmd-9-1153-2016, 2016.

Kim, J. H. and Lee, H.: What causes the springtime tropospheric ozone maximum over Northeast Asia?, Adv. Atmos. Sci., 27, 543-551, https://doi.org/10.1007/s00376-009-9098-z, 2010.

Kluge, F., Hüneke, T., Lerot, C., Rosanka, S., Rotermund, M. K., Taraborrelli, D., Weyland, B., and Pfeilsticker, K.: Airborne glyoxal measurements in the marine and continental atmosphere: comparison with TROPOMI observations and EMAC simulations, Atmos. Chem. Phys., 23, 1369-1401, https://acp.copernicus.org/articles/23/1369/2023, 2023.

Lalitaporn, P.: Long-Term Assessment of Carbon Monoxide Using MOPITT Satellite and Surface Data over Thailand., Eng. Appl. Sci. Res., 45, 132-139, https://doi.org/10.14456/EASR.2018.17, 2018.

Lalitaporn, P. and Boonmee, T.: Analysis of Tropospheric Nitrogen Dioxide Using Satellite and Ground Based Data over Northern Thailand, Eng. J., 23, 19-35, https://doi.org/10.4186/ej.2019.23.6.19, 2019.

Lee, H. N., Tositti, L., Zheng, X., and Bonasoni, P.: Analyses and comparisons of variations of 7Be, 210Pb, and 7Be/210Pb with ozone observations at two Global Atmosphere Watch stations from high mountains, J. Geophys. Res.-Atmos., 112, 1–11, https://doi.org/10.1029/2006JD007421, 2007.

Lefohn, A. S., Malley, C. S., Smith, L., Wells, B., Hazucha, M., Simon, H., Naik, V., Mills, G., Schultz, M. G., Paoletti, E., De Marco, A., Xu, X., Zhang, L., Wang, T., Neufeld, H. S., Musselman, R. C., Tarasick, D., Brauer, M., Feng, Z., Tang, H., Kobayashi, K., Sicard, P., Solberg, S., and Gerosa, G.: Tropospheric ozone assessment report: Global

ozone metrics for climate change, human health, and crop/ecosystem research, Elem. Sci. Anth., 6, 28, https://doi.org/10.1525/elementa.279, 2018.

Lelieveld, J. and Dentener, F. J.: What controls tropospheric ozone?, J. Geophys. Res.-Atmos., 105, 3531-3551, https://doi.org/10.1029/1999JD901011, 2000.

Lelieveld, J., Gromov, S., Pozzer, A., and Taraborrelli, D.: Global tropospheric hydroxyl distribution, budget and reactivity, Atmos. Chem. Phys., 16, 12477-12493, https://doi.org/10.5194/acp-16-12477-2016, 2016.

Levy, H.: Normal Atmosphere - Large Radical and Formaldehyde Concentrations Predicted, Science, 173, 141-143, https://doi.org/10.1126/science.173.3992.141, 1971.

Li, J., Wang, Z., Akimoto, H., Tang, J., and Uno, I.: Modeling of the impacts of China's anthropogenic pollutants on the surface ozone summer maximum on the northern Tibetan Plateau, Geophys. Res. Lett., 36, https://doi.org/10.1029/2009GL041123, 2009.

Li, K., Tan, R., Qiao, W., Lee, T., Wang, Y., Zhang, D., Tang, M., Zhao, W., Gu, Y., Fan, S., Zhang, J., Lyu, X., Xue, L., Xu, J., Ma, Z., Latif, M. T., Amnuaylojaroen, T., Gil, J., Lee, M. H., Bak, J., Kim, J., Liao, H., Kanaya, Y., Lu, X., Nagashima, T., and Koo, J. H.: Surface and tropospheric ozone over East Asia and Southeast Asia from observations: distributions, trends, and variability, Atmos. Chem. Phys., 25, 11575-11596, https://doi.org/10.5194/acp-25-11575-2025, 2025.

Li, M., Yang, Y., Wang, H., Li, H., Wang, P., and Liao, H.: Summertime ozone pollution in China affected by stratospheric quasi-biennial oscillation, Atmos. Chem. Phys., 23, 1533-1544, https://doi.org/10.5194/acp-23-1533-2023, 2023.

Li, X., Liu, J., Mauzerall, D. L., Emmons, L. K., Walters, S., Horowitz, L. W., and Tao, S.: Effects of trans-Eurasian transport of air pollutants on surface ozone concentrations over Western China, J. Geophys. Res.-Atmos., 119, 12,338-312,354, https://doi.org/10.1002/2014JD021936, 2014.

Li, Y., Feng, W., Zhou, X., Li, Y., and Chipperfield, M. P.: The impact of El Niño–Southern Oscillation on the total column ozone over the Tibetan Plateau, Atmos. Chem. Phys., 24, 8277-8293, https://doi.org/10.5194/acp-24-8277-2024, 2024.

Liang, M.-C., Tang, J., Chan, C.-Y., Zheng, X. D., and Yung, Y. L.: Signature of stratospheric air at the Tibetan Plateau, Geophys. Res. Lett., 35, L20816, https://doi.org/10.1029/2008GL035246, 2008.

Lin, M., Zhang, Z., Su, L., Hill-Falkenthal, J., Priyadarshi, A., Zhang, Q., Zhang, G., Kang, S., Chan, C.-Y., and Thiemens, M. H.: Resolving the impact of stratosphere-to-troposphere transport on the sulfur cycle and surface ozone over the Tibetan Plateau using a cosmogenic 35S tracer, J. Geophys. Res.-Atmos., 121, 439-456, https://doi.org/10.1002/2015JD023801, 2016.

Lin, W., Xu, X., Zheng, X., Dawa, J., Baima, C., and Ma, J.: Two-year measurements of surface ozone at Dangxiong, a remote highland site in the Tibetan Plateau, J. Environ. Sci., 31, 133-145, https://doi.org/10.1016/j.jes.2014.10.022, 2015.

Liu, N., Ma, J., Xu, W., Wang, Y., Pozzer, A., and Lelieveld, J.: A modeling study of the regional representativeness of surface ozone variation at the WMO/GAW background stations in China, Atmos. Environ., 242, 117672, https://doi.org/10.1016/j.atmosenv.2020.117672, 2020.

Lu, X., Zhang, L., Liu, X., Gao, M., Zhao, Y., and Shao, J.: Lower tropospheric ozone over India and its linkage to the South Asian monsoon, Atmos. Chem. Phys., 18, 3101-3118, https://doi.org/10.5194/acp-18-3101-2018, 2018.

Luo, J., Liang, W., Xu, P., Xue, H., Zhang, M., Shang, L., and Tian, H.: Seasonal Features and a Case Study of Tropopause Folds over the Tibetan Plateau, Adv. Meteorol., 2019, 4375123, https://doi.org/10.1155/2019/4375123, 2019.

Ma, J., Liu, H., and Hauglustaine, D.: Summertime tropospheric ozone over China simulated with a regional chemical transport model 1. Model description and evaluation, J. Geophys. Res.-Atmos., 107, ACH 27-21-ACH 27-13, https://doi.org/10.1029/2001JD001354, 2002a.

Ma, J., Tang, J., Zhou, X., and Zhang, X.: Estimates of the Chemical Budget for Ozone at Waliguan Observatory, J. Atmos. Chem., 41, 21-48, https://doi.org/10.1023/A:1013892308983, 2002b.

Ma, J., Zhou, X., and Hauglustaine, D.: Summertime tropospheric ozone over China simulated with a regional chemical transport model 2. Source contributions and budget, J. Geophys. Res.-Atmos., 107, ACH 2-1-ACH 2-11, https://doi.org/10.1029/2001JD001354, 2002c.

Ma, J., Zheng, X., and Xu, X.: Comment on “Why does surface ozone peak in summertime at Waliguan?” by Bin Zhu et al, Geophys. Res. Lett., 32, L01805, https://doi.org/10.1029/2004GL021683, 2005.

Ma, J., Lin, W. L., Zheng, X. D., Xu, X. B., Li, Z., and Yang, L. L.: Influence of air mass downward transport on the variability of surface ozone at Xianggelila Regional Atmosphere Background Station, southwest China, Atmos. Chem. Phys., 14, 5311-5325, https://doi.org/10.5194/acp-14-5311-2014, 2014.

Ma, J., Brühl, C., He, Q., Steil, B., Karydis, V. A., Klingmüller, K., Tost, H., Chen, B., Jin, Y., Liu, N., Xu, X., Yan, P., Zhou, X., Abdelrahman, K., Pozzer, A., and Lelieveld, J.: Modeling the aerosol chemical composition of the tropopause over the Tibetan Plateau during the Asian summer monsoon, Atmos. Chem. Phys., 19, 11587-11612, https://doi.org/10.5194/acp-19-11587-2019, 2019.

Ma, J., Zhou, X., Xu, X., Xu, X., Gromov, S., and Lelieveld, J.: Chapter 15 - Ozone and aerosols over the Tibetan Plateau, in: Asian Atmospheric Pollution, edited by: Singh, R. P., Elsevier, 287-302, https://doi.org/10.1016/B978-0-12-816693-2.00008-1, 2022.

Marinoni, A., Cristofanelli, P., Laj, P., Duchi, R., Putero, D., Calzolari, F., Landi, T. C., Vuillermoz, E., Maione, M., and Bonasoni, P.: High black carbon and ozone concentrations during pollution transport in the Himalayas: Five years of continuous observations at NCO-P global GAW station, J. Environ. Sci., 25, 1618-1625, https://doi.org/10.1016/S1001-0742(12)60242-3, 2013.

Monks, P. S., Archibald, A. T., Colette, A., Cooper, O., Coyle, M., Derwent, R., Fowler, D., Granier, C., Law, K. S., Mills, G. E., Stevenson, D. S., Tarasova, O., Thouret, V., Schneidemesser, E. v., Sommariva, R., Wild, O., and Williams, M. L.: Tropospheric ozone and its precursors from the urban to the global scale from air quality to short-lived climate forcer, Atmos. Chem. Phys., 15, 8889-8973, https://doi.org/10.5194/acp-15-8889-2015, 2015.

Myhre, G., Shindell, D., Bréon, F.-M., Collins, W., Fuglestvedt, J., Huang, J., Koch, D., Lamarque, J.-F., Lee, D., Mendoza, B., Nakajima, T., Robock, A., Stephens, G., Takemura, T., and Zhang, H.: Anthropogenic and Natural Radiative Forcing, in: Climate Change 2013: The Physical Science Basis. Contribution of Working Group I to the Fifth Assessment Report of the Intergovernmental Panel on Climate Change, Cambridge University Press, Cambridge, United Kingdom and New York, NY, USA, 659–740, https://doi.org/10.1017/CBO9781107415324.018, 2013.

Ni, Z.-Z., Luo, K., Gao, X., Gao, Y., Fan, J.-R., Fu, J. S., and Chen, C.-H.: Exploring the stratospheric source of ozone pollution over China during the 2016 Group of Twenty summit, Atmos. Pollut. Res., 10, 1267-1275, https://doi.org/10.1016/j.apr.2019.02.010, 2019.

Oltmans, S. J., Hofmann, D. J., Lathrop, J. A., Harris, J. M., Komhyr, W. D., and Kuniyuki, D.: Tropospheric ozone during Mauna Loa Observatory Photochemistry Experiment 2 compared to long-term measurements from surface and ozonesonde observations, J. Geophys. Res.-Atmos., 101, 14569-14580, https://doi.org/10.1029/95JD03004, 1996.

Pozzer, A., Jöckel, P., and Van Aardenne, J.: The influence of the vertical distribution of emissions on tropospheric chemistry, Atmos. Chem. Phys., 9, 9417-9432, https://doi.org/10.5194/acp-9-9417-2009, 2009.

Pozzer, A., de Meij, A., Yoon, J., Tost, H., Georgoulias, A. K., and Astitha, M.: AOD trends during 2001–2010 from observations and model simulations, Atmos. Chem. Phys., 15, 5521-5535, https://doi.org/10.5194/acp-15-5521-2015, 2015.

Putero, D., Landi, T. C., Cristofanelli, P., Marinoni, A., Laj, P., Duchi, R., Calzolari, F., Verza, G. P., and Bonasoni, P.: Influence of open vegetation fires on black carbon and ozone variability in the southern Himalayas (NCO-P, 5079 m a.s.l.), Environ. Pollut., 184, 597-604, https://doi.org/10.1016/j.envpol.2013.09.035, 2014.

Ramanathan, V., Callis, L., Cess, R., Hansen, J., Isaksen, I., Kuhn, W., Lacis, A., Luther, F., Mahlman, J., Reck, R., and Schlesinger, M.: Climate-chemical interactions and effects of changing atmospheric trace gases, Rev. Geophys., 25, 1441-1482, https://doi.org/10.1029/RG025i007p01441, 1987.

Ran, L., Lin, W. L., Deji, Y. Z., La, B., Tsering, P. M., Xu, X. B., and Wang, W.: Surface gas pollutants in Lhasa, a highland city of Tibet - current levels and pollution implications, Atmos. Chem. Phys., 14, 10721-10730, https://doi.org/10.5194/acp-14-10721-2014, 2014.

Roelofs, G.-J. and Lelieveld, J.: Model study of the influence of cross-tropopause O_3 transports on tropospheric O_3 levels, Tellus B, 49, 38-55, https://doi.org/10.3402/tellusb.v49i1.15949, 1997.

Schiemann, R., Lüthi, D., and Schär, C.: Seasonality and Interannual Variability of the Westerly Jet in the Tibetan Plateau Region, J. Climate, 22, 2940-2957, https://doi.org/10.1175/2008JCLI2625.1, 2009.

Shindell, D., Kuylenstierna, J. C. I., Vignati, E., van Dingenen, R., Amann, M., Klimont, Z., Anenberg, S. C., Muller, N., Janssens-Maenhout, G., Raes, F., Schwartz, J., Faluvegi, G., Pozzoli, L., Kupiainen, K., Höglund-Isaksson, L., Emberson, L., Streets, D., Ramanathan, V., Hicks, K., Oanh, N. T. K., Milly, G., Williams, M., Demkine, V., and

Fowler, D.: Simultaneously Mitigating Near-Term Climate Change and Improving Human Health and Food Security, Science, 335, 183-189, https://doi.org/10.1126/science.1210026, 2012.

Škerlak, B., Sprenger, M., and Wernli, H.: A global climatology of stratosphere–troposphere exchange using the ERA-Interim data set from 1979 to 2011, Atmos. Chem. Phys., 14, 913-937, https://doi.org/10.5194/acp-14-913-2014, 2014.

Škerlak, B., Sprenger, M., Pfahl, S., Tyrlis, E., and Wernli, H.: Tropopause folds in ERA-Interim: Global climatology and relation to extreme weather events, J. Geophys. Res.-Atmos., 120, 4860-4877, https://doi.org/10.1002/2014JD022787, 2015.

Stohl, A., Bonasoni, P., Cristofanelli, P., Collins, W., Feichter, J., Frank, A., Forster, C., Gerasopoulos, E., Gäggeler, H., James, P., Kentarchos, T., Kromp-Kolb, H., Krüger, B., Land, C., Meloen, J., Papayannis, A., Priller, A., Seibert, P., Sprenger, M., Roelofs, G. J., Scheel, H. E., Schnabel, C., Siegmund, P., Tobler, L., Trickl, T., Wernli, H., Wirth, V., Zanis, P., and Zerefos, C.: Stratosphere-troposphere exchange: A review, and what we have learned from STACCATO, J. Geophys. Res.-Atmos., 108, https://doi.org/10.1029/2002JD002490, 2003.

Sukkhum, S., Lim, A., Ingviya, T., and Saelim, R.: Seasonal Patterns and Trends of Air Pollution in the Upper Northern Thailand from 2004 to 2018, Aerosol Air Qual. Res., 22, 210318, https://doi.org/10.4209/aaqr.210318, 2022.

Tang, J., Wen, Y. P., Xu, X. B., Zheng, X. D., Guo, S., and Zhao, Y. C.: China Global Atmosphere Watch Baseline Observatory and its measurement program, in: CAMS Annual Report 1994–1995, China Meteorological Press, Beijing, 56–65, 1995.

Tang, Q., Prather, M. J., and Hsu, J.: Stratosphere-troposphere exchange ozone flux related to deep convection, Geophys. Res. Lett., 38, L03806, https://doi.org/10.1029/2010GL046039, 2011.

Tarasick, D., Galbally, I. E., Cooper, O. R., Schultz, M. G., Ancellet, G., Leblanc, T., Wallington, T. J., Ziemke, J., Liu, X., Steinbacher, M., Staehelin, J., Vigouroux, C., Hannigan, J. W., García, O., Foret, G., Zanis, P., Weatherhead, E., Petropavlovskikh, I., Worden, H., Osman, M., Liu, J., Chang, K.-L., Gaudel, A., Lin, M., Granados-Muñoz, M., Thompson, A. M., Oltmans, S. J., Cuesta, J., Dufour, G., Thouret, V., Hassler, B., Trickl, T., and Neu, J. L.: Tropospheric Ozone Assessment Report: Tropospheric ozone from 1877 to 2016, observed levels, trends and uncertainties, Elem. Sci. Anth., 7, 39, https://doi.org/10.1525/elementa.376, 2019.

Vingarzan, R.: A review of surface ozone background levels and trends, Atmos. Environ., 38, 3431-3442, https://doi.org/10.1016/j.atmosenv.2004.03.030, 2004.

Wang, X., Fu, T.-M., Zhang, L., Lu, X., Liu, X., Amnuaylojaroen, T., Latif, M. T., Ma, Y., Zhang, L., Feng, X., Zhu, L., Shen, H., and Yang, X.: Rapidly Changing Emissions Drove Substantial Surface and Tropospheric Ozone Increases Over Southeast Asia, Geophys. Res. Lett., 49, e2022GL100223, https://doi.org/10.1029/2022GL100223, 2022.

Weinstock, B. and Niki, H.: Carbon-Monoxide Balance in Nature, Science, 176, 290-292, https://doi.org/10.1126/science.176.4032.290, 1972.

Xu, W., Lin, W., Xu, X., Tang, J., Huang, J., Wu, H., and Zhang, X.: Long-term trends of surface ozone and its influencing factors at the MtWaliguan GAW station, China – Part 1: Overall trends and characteristics, Atmos. Chem. Phys., 16, 6191-6205, https://doi.org/10.5194/acp-16-6191-2016, 2016.

Xu, W., Xu, X., Lin, M., Lin, W., Tarasick, D., Tang, J., Ma, J., and Zheng, X.: Long-term trends of surface ozone and its influencing factors at the Mt Waliguan GAW station, China – Part 2: The roles of anthropogenic emissions and climate variability, Atmos. Chem. Phys., 18, 773-798, https://doi.org/10.5194/acp-18-773-2018, 2018a.

Xu, W., Bian, Y., Lin, W., Zhang, Y., Wang, Y., Ma, Z., Zhang, X., Zhang, G., Ye, C., and Xu, X.: O3 and PAN in southern Tibetan Plateau determined by distinct physical and chemical processes, Atmos. Chem. Phys., 23, 7635-7652, https://doi.org/10.5194/acp-23-7635-2023, 2023.

Xu, X., Zhang, H., Lin, W., Wang, Y., Xu, W., and Jia, S.: First simultaneous measurements of peroxyacetyl nitrate (PAN) and ozone at Nam Co in the central Tibetan Plateau: impacts from the PBL evolution and transport processes, Atmos. Chem. Phys., 18, 5199-5217, https://doi.org/10.5194/acp-18-5199-2018, 2018b.

Xue, L., Ding, A., Cooper, O., Huang, X., Wang, W., Zhou, D., Wu, Z., McClure-Begley, A., Petropavlovskikh, I., Andreae, M. O., and Fu, C.: ENSO and Southeast Asian biomass burning modulate subtropical trans-Pacific ozone transport, Natl. Sci. Rev, 8, https://doi.org/10.1093/nsr/nwaa132, 2020.

Xue, L. K., Wang, T., Zhang, J. M., Zhang, X. C., Deliger, Poon, C. N., Ding, A. J., Zhou, X. H., Wu, W. S., Tang, J., Zhang, Q. Z., and Wang, W. X.: Source of surface ozone and reactive nitrogen speciation at Mount Waliguan in western

China: New insights from the 2006 summer study, J. Geophys. Res.-Atmos., 116, https://doi.org/10.1029/2010JD014735, 2011.

Yang, J., Kang, S., Hu, Y., Chen, X., and Rai, M.: Influence of South Asian Biomass Burning on Ozone and Aerosol Concentrations Over the Tibetan Plateau, Adv. Atmos. Sci., 39, 1184-1197, https://doi.org/10.1007/s00376-022-1197-0, 2022.

Ye, X., Zhang, L., Wang, X., Lu, X., Jiang, Z., Lu, N., Li, D., and Xu, J.: Spatial and temporal variations of surface background ozone in China analyzed with the grid-stretching capability of GEOS-Chem High Performance, Sci. Total Environ., 914, 169909, https://doi.org/10.1016/j.scitotenv.2024.169909, 2024.

Yin, X., Kang, S., de Foy, B., Cong, Z., Luo, J., Zhang, L., Ma, Y., Zhang, G., Rupakheti, D., and Zhang, Q.: Surface ozone at Nam Co in the inland Tibetan Plateau: variation, synthesis comparison and regional representativeness, Atmos. Chem. Phys., 17, 11293-11311, https://doi.org/10.5194/acp-17-11293-2017, 2017.

Yin, X., Rupakheti, D., Zhang, G., Luo, J., Kang, S., de Foy, B., Yang, J., Ji, Z., Cong, Z., Rupakheti, M., Li, P., Hu, Y., and Zhang, Q.: Surface ozone over the Tibetan Plateau controlled by stratospheric intrusion, Atmos. Chem. Phys., 23, 10137-10143, https://doi.org/10.5194/acp-23-10137-2023, 2023.

Yoshitomi, M., Wild, O., and Akimoto, H.: Contributions of regional and intercontinental transport to surface ozone in the Tokyo area, Atmos. Chem. Phys., 11, 7583-7599, https://doi.org/10.5194/acp-11-7583-2011, 2011.

Young, P. J., Naik, V., Fiore, A. M., Gaudel, A., Guo, J., Lin, M. Y., Neu, J. L., Parrish, D. D., Rieder, H. E., Schnell, J. L., Tilmes, S., Wild, O., Zhang, L., Ziemke, J. R., Brandt, J., Delcloo, A., Doherty, R. M., Geels, C., Hegglin, M. I., Hu, L., Im, U., Kumar, R., Luhar, A., Murray, L., Plummer, D., Rodriguez, J., Saiz-Lopez, A., Schultz, M. G., Woodhouse, M. T., and Zeng, G.: Tropospheric Ozone Assessment Report: Assessment of global-scale model performance for global and regional ozone distributions, variability, and trends, Elem. Sci. Anth., 6, 10, https://doi.org/10.1525/elementa.265, 2018.

Zhao, K., Hu, C., Yuan, Z., Xu, D., Zhang, S., Luo, H., Wang, J., and Jiang, R.: A modeling study of the impact of stratospheric intrusion on ozone enhancement in the lower troposphere over the Hong Kong regions, China, Atmos. Res., 247, 105158, https://doi.org/10.1016/j.atmosres.2020.105158, 2021a.

Zhao, K., Huang, J., Wu, Y., Yuan, Z., Wang, Y., Li, Y., Ma, X., Liu, X., Ma, W., Wang, Y., and Zhang, X.: Impact of Stratospheric Intrusions on Ozone Enhancement in the Lower Troposphere and Implication to Air Quality in Hong Kong and Other South China Regions, J. Geophys. Res.-Atmos., 126, e2020JD033955, https://doi.org/10.1029/2020JD033955, 2021b.

Zheng, X., Shen, C., Wan, G., Liu, K., Tang, J., and Xu, X.: 10Be/7Be implies the contribution of stratosphere-troposphere transport to the winter-spring surface O3 variation observed on the Tibetan Plateau, Chin. Sci. Bull., 56, 84-88, https://doi.org/10.1007/s11434-010-4211-3, 2011.

Zhu, B., Akimoto, H., Wang, Z., Sudo, K., Tang, J., and Uno, I.: Why does surface ozone peak in summertime at Waliguan?, Geophys. Res. Lett., 31, https://doi.org/10.1029/2004GL020609, 2004.